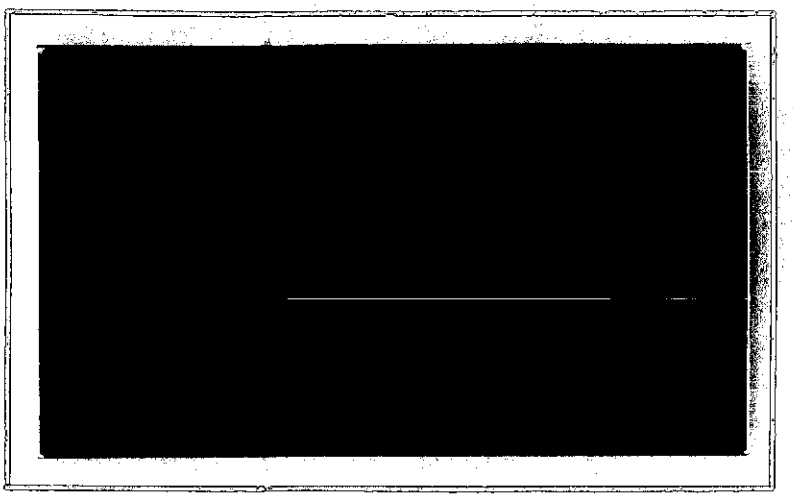

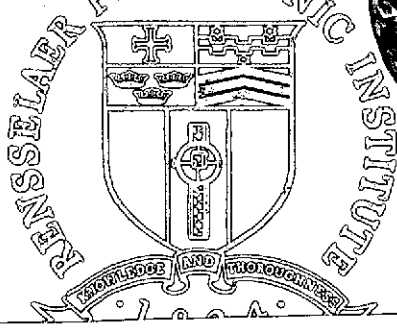

Rensselaer Polytechnic Institute

Troy, New York 12181

R.P.I. Technical Report MP-45

RECOGNITION OF THREE DIMENSIONAL OBSTACLES BY AN EDGE DETECTION SCHEME

by

Martin A. Reed

NASA GRANT NGL 33-018-091

Analysis and Design of a Capsule Landing System
and Surface Vehicle Control System for Mars Exploration

Rensselaer Polytechnic Institute
Troy, New York

May 1974

TABLE OF CONTENTS

LIST OF FIGURES

LIST OF TABLES

ACKNOWLEDGMENT

I wish to express the sincerest gratitude to my advisor Dr. C.N. Shen, whose continued guidance and helpful suggestions provided the motivation for this project.

ABSTRACT

The need for an obstacle detection system on the Mars roving vehicle was assumed, and a practical scheme was therefore investigated and simulated. The principal sensing device on this vehicle was taken to be a laser range finder. Both existing and original algorithms, ending with thresholding operations, were used to obtain the outlines of obstacles from the raw data of this laser scan. A theoretical analysis was carried out to show how proper value of threshold may be chosen. Computer simulations considered various mid-range boulders, for which the scheme was quite successful. The extension to other types of obstacles, such as craters, was considered. The special problems of bottom edge detection and scanning procedure are discussed.

INTRODUCTION

The proposed Mars Rover which may be landed on the surface of Mars in the early 1980's will be required to navigate autonomously to reach preset destinations [1, 2]. The possibility of remotely controlling the vehicle from Earth, as can be done in the case of a vehicle on the Moon, is ruled out for the Mars Rover, because the round trip communication time between Earth and Mars is approximately 40 minutes. With this much time lag it is all but impossible to control a vehicle that is expected to move at a nominal speed of about 1 meter/second.

As far as possible, an optimum feasible path for the Rover to travel between point of landing and other points of interest on the Martian surface will be predetermined from the aerial maps available so far. However, many objects, which can be potential obstacles for the Rover, may be small enough not to show up on the pictures. It is expected that there will be obstacles in the form of boulders, craters, slopes, etc., which will be small enough not to be seen. Therefore, it is desired that the Rover be equipped with its own obstacle detection system.

Much research has been done and is being done on robots which incorporate some form of primitive "brain" and are thus able to "see". Unfortunately, these systems are much too complicated to be installed on the Mars Rover, where weight and reliability are among the paramount considerations. Thus, a system is being sought that will be simple, requiring less bulky sensors and smaller computer memory space. This paper discusses one such system.

1. HARDWARE CHOICE

It has been decided that a laser range finder will be the primary sensing device on the Rover. The "time of flight" technique will be used for the determination of range. This means that at given time intervals a laser pulse will be sent out towards the terrain in front of the vehicle, and will be reflected back from the surface it impinges on to a laser detector. The time difference between transmitted and reflected beams will indicate the range.

As far as the laser range finder is concerned, the following requirements must be met: [3]

1) Accurate enough for reliable processing, i.e, $\pm$ 5 cm for range error and $\pm$ 10 arc seconds for angle error.
2) Fast scan capabilities.
3) Light weight.
4) Low power consumption.

The first two of these are applicable to the research discussed in this paper. The range error was taken into account by adding gaussian noise, with zero mean and 5 cm standard deviation, to the geometrically derived range values used in the computer simulation. The angle error was neglected in this work, since the specified 10 arc seconds is about two orders of magnitude smaller than the smallest angles used. With regard to fast scan capabilities, it is expected that the time required per range readings will not exceed 1 millisecond. Thus in .5 seconds, or in the space of .5 meters traveled by the Rover, about 500 range

readings can be obtained. This is the approximate number of readings used in the simulation, where, however, it has been assumed that all readings have been obtained with the vehicle stationary. This assumption will have to be re-examined in future extensions of the edge detection scheme.

One final piece of hardware information is that the laser scan is assumed to be mounted on a vertical mast attached to the front of the vehicle, at a height of 3 meters from ground level. This number may be easily changed in the simulation program, as physical requirements dictate. It is felt that the success of the edge detection scheme is relatively insensitive to changes in the mast height, and no problems should arise as a result of it.

2. PROBLEM DEFINITION

2.1 Objectives of Simulation vs. Implementation

Throughout this paper, the distinctions between simulation objectives and implementation objectives should always be kept in mind. The steps involved in simulation are as follows:

(a) A realistic terrain model, including the obstacle or obstacles to be detected, must be envisioned and mathematically modelled.

(b) The range values must be generated, based on the geometry of the model (see Section 2.2).

(c) Thresholds to be used in the edge detection algorithms are calculated.

(d) Expected values of noise in the laser measurement process must be added to the range values.

(e) Algorithms are then used to operate on the noisy range measurements to obtain an outline of the obstacles, based on the pre-selected thresholds.

The end result of this process is an evaluation of the quality of reproduction of the edge of the obstacle, for differing combinations of threshold choice, algorithm choice, and scan angle choices.

In the implementation, the procedure for the on-board computer is:

(a) Obtain the noisy range values from the laser scan, where the scan angles have been determined from the simulation results.

(b) Operate on these values, using pre-stored algorithms and thresholds (or procedures for finding thresholds) selected as optimum from simulation results, to determine the size and location of any obstacles.

The end result of this process is a path selection decision [4].

The research presented in this paper, while interesting in itself, was primarily directed towards realization of the final system. In this respect, emphasis has been placed on obtaining results in the areas common to the simulation and implementation, i.e., threshold and algorithm evaluation. The preliminary work should therefore be seen as just that - steps leading up to this goal.

2.2 Geometrical Considerations

Figure 1 illustrates a simplified picture of the Mars Rover, with a positive obstacle (one that projects above the ground level, such as a boulder) directly in its path of travel. The Martian surface is taken to be perfectly flat here and in all simulations. One reason for this choice is to simplify calculations and to limit the number of independent variables in this preliminary development. In addition, research is currently being carried on in the development of a terrain modeling procedure, [5, 6] where sloped terrains are being considered, so it was not felt necessary to duplicate this effort until the edge detection scheme becomes more refined.

As shown, β (the elevation angle) is defined to be the angle between the laser beam and the normal to the laser mast, θ (the azimuth angle) is defined to be the angle between the laser beam and the line representing the Rover's direction of travel, and b is defined to be the horizontal distance from the laser mast to the center of the obstacle (when such a center point exists).

The obstacle considered for most of this work was a hemi-

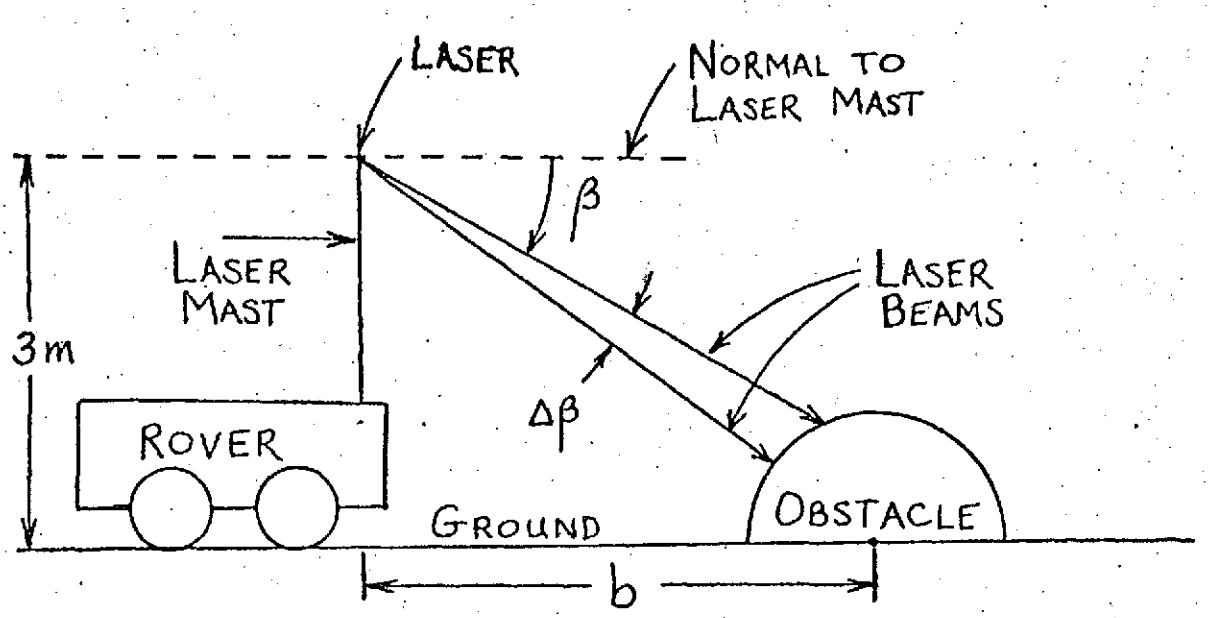

(a) Side View

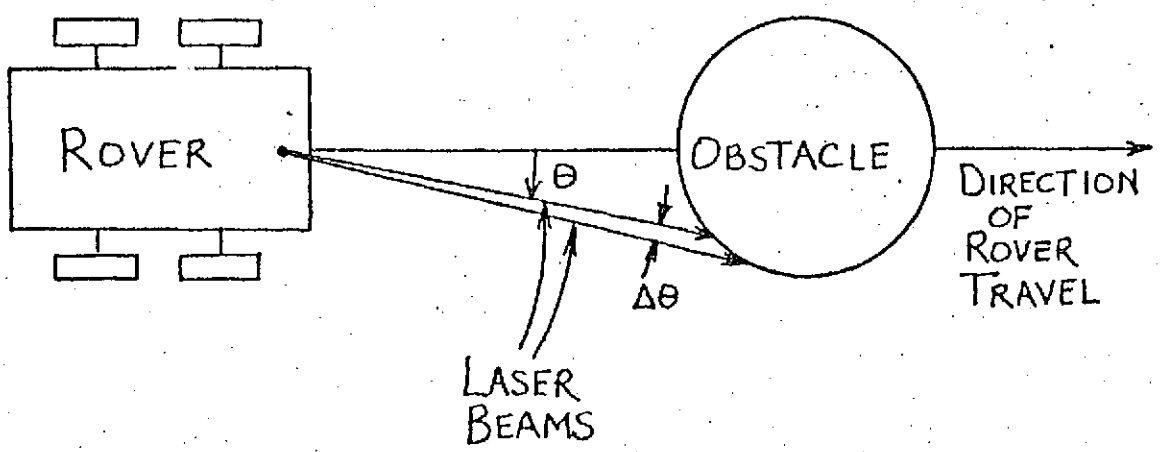

(b) Top View

FIGURE 1

Scenario of Problem Studies

spherical boulder of radius r, whose center was located on the ground, directly in the vehicle's path of travel, at a horizontal distance of b meters from the laser mast. In order to generate the range values, as functions of b, r, β, and θ, a more detailed geometry was defined. Referring to figure 2, the origin of the x, y', z axes is located on the ground directly below the laser, which is the point (0,0,3) therefore. The origin of the x, y, z axis is located at the center of the boulder, so that (0,0,0) in the x, y, z frame is the same as (0,b,0) in the x, y', z frame. The beam from the laser to the point of impingement on the boulder if R_1, and the radius from the center of the boulder to the point of impingement is r. The other variables are introduced merely for convenience in the calculations.

Assuming the laser beam has hit the boulder, the following equations enable us to calculate the range R_1:

$$x = R_1 \sin \theta \tag{1}$$

$$z = R_2 \sin \beta \tag{2}$$

$$R_2 = \frac{3}{\sin \beta} - R_1 \tag{3}$$

Substituting (3) into (2)

$$z = 3 - R_1 \sin \beta \tag{4}$$

$$R_{xy2} = R_2 \cos \beta \tag{5}$$

$$R_{xy2} = \frac{3}{\tan \beta} - R_{xy1} \tag{6}$$

$$R_{xy1} = \sqrt{(y+b)^2 + x^2} \tag{7}$$

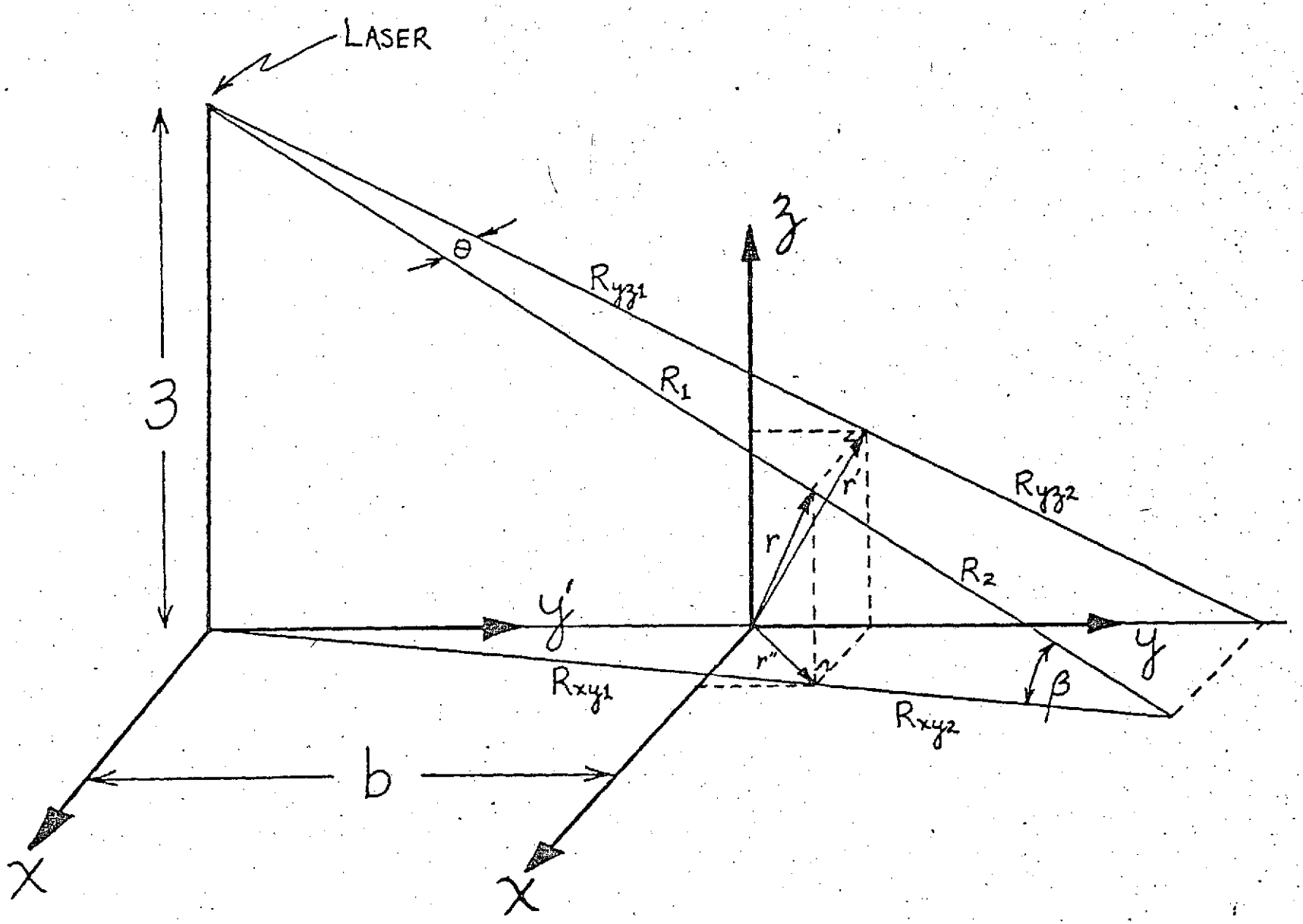

FIGURE 2

Geometry for Calculation of Range Values to a Boulder

Substituting (3), (6), and (7) into (5)

$$\sqrt{(y + b)^2 + x^2} = R_1 \cos \beta \tag{8}$$

Manipulating (8) we find that

$$y = R_1(\cos^2\beta - \sin^2\theta) - 2bR_1\sqrt{\cos^2\beta - \sin^2\theta} + b^2 \tag{9}$$

The equation of a sphere is:

$$x^2 + y^2 + z^2 = r^2 \tag{10}$$

Squaring (1), (2), and (9), substituting into (10) and simplifying,

$$R_1^2 + R_1 \left(-2b\sqrt{\cos^2\beta - \sin^2\theta} - 6\sin\beta\right) + (b^2 + 9 - r^2) = 0 \tag{11}$$

This is a quadratic equation in R_1, and one of its solutions (the smaller one of course, since the larger solution indicates that the laser beam has passed through the sphere and contacted the surface on the other side) is the range value we are seeking. Notice that we have the desired functional dependence on b, r, β, and θ.

The other possibility is that the laser beam hits the terrain surrounding the boulder. In this case the range is actually independent of θ (and, of course, b) and is simply expressed as,

$$R_1 = \frac{3}{\sin \beta} \tag{12}$$

At this stage, by specifying b and r, and by sweeping β and θ through limits to include the entire boulder, we can generate a matrix of range values. These values are the input to the edge detection algorithms.

3. EDGE DETECTION SYSTEM

3.1 The Scan

The range data $z_{i,j}$ (composed of the geometrically derived values given by equations (11) and (12), plus the additive Gaussian noise term) which is obtained by varying the angles β and θ, can be stored in computer memory in a matrix form with the elements ordered according to the values of β and θ. The value of θ changes along each row with the index j, while the value of β changes along each column with the index i. This matrix Z, called the measurement matrix, forms a range image of the scene ahead. In contrast to a photographic image, where the elements of the image are functions of the brightness of the scene, the range image consists of distances of the points on the scene from the point of measurement. The measurement matrix is thus represented as:

$$Z = \begin{bmatrix} z_{11} & z_{12} & \cdots & \cdots & \cdots & z_{1n} \\ \vdots & & & z_{i-1,j} & & \vdots \\ \cdots & z_{i,j-1} & z_{i,j} & z_{i,j+1} & & \cdots \\ \vdots & & & z_{i+1,j} & & \vdots \\ z_{m1} & z_{m2} & \cdots & \cdots & \cdots & z_{mn} \end{bmatrix} \tag{13}$$

Once again, the values in this matrix will all be directly measured by the laser range finder and stored in the on-board computer in the actual operating system.

3.2 The Sharp Changes in Range Readings

Whenever adjacent elements of the measurement matrix are all

taken from the same terrain feature, e.g. several neighboring points on a flat terrain or several neighboring points on the side of a relatively continuous obstacle, then the range readings of these points will vary only slightly from each other, especially when the differences in elevation and azimuth angles measured from the laser to the points is small. And in the case of two or more points on a flat terrain with the same elevation angle, the range readings will be exactly the same (discounting noise), as shown by equation (12). However, adjacent elements which straddle the edge of an obstacle (one measuring the range close to the obstacle's edge, and the other measuring the range to the terrain, with this latter beam passing just outside the obstacle's edge) often exhibit sharp changes in range, which can be used to indicate the presence of the edge. This physical property is the basis of the edge detection scheme.

A means is required to bring out or enhance these sharp changes in range readings, in order to recognize the edges. Therefore, algorithms were sought which involved fairly simple manipulations of the range values (to minimize computation time required by the small, on-board computer, so that path selection decisions can be made as soon after determination of the range image as possible), evaluated a test point in relationship to its four surrounding "neighbors" in the range image (so that an edge in any orientation near the test point would be detected), and ended with a thresholding operation (to provide the necessary numerical cutoff indication between the presence and absence of an edge). The success of the algorithms depends on the quality of the enhanced edge, once the

optimum thresholds have been selected, and on the relative ease with which the proper thresholds can be selected.

3.3 Algorithms Used

Based on the preceding criteria, the following two algorithms were selected for use in the simulations. Their merits and drawbacks will be discussed and illustrated.

(a) Normalized Laplacian [7]

A new matrix Q can be obtained by the following operation on the range values:

$$q_{i,j} = \frac{z_{i-1,j}+z_{i+1,j}+z_{i,j-1}+z_{i,j+1}-4z_{i,j}}{z_{i-1,j}+z_{i+1,j}+z_{i,j-1}+z_{i,j+1}} \qquad (14)$$

(b) Four Directional Ratio

A new matrix S is obtained by operating on the range values as below:

$$s_{i,j} = \frac{1}{4}\left(\frac{z_{i-1,j}}{z_{i,j}}\right)^n + \left(\frac{z_{i+1,j}}{z_{i,j}}\right)^n + \left(\frac{z_{i,j-1}}{z_{i,j}}\right)^n + \left(\frac{z_{i,j+1}}{z_{i,j}}\right)^n \qquad (15)$$

The Normalized Laplacian is from the existing literature, while the Four Directional Ratio was developed specifically for this application.

3.4 Analysis of the Algorithms [8]

The purpose of this section is to develop a procedure for choosing the proper values of threshold for each algorithm, given the type of irregularity to be detected, and to analyze the effects of noise on the measurement data for a determination of how large the statistics of noise can be allowed without leading to false alarms. In order to

reach these two objectives, each contribution to the range measurements will be derived separately.

Let

$$z_{i,j} = r_{i,j} + v_{i,j} \tag{16}$$

where $r_{i,j}$ is the true range measurement, $v_{i,j}$ is the additive noise term, and $z_{i,j}$ is the resulting range value as measured by the laser rangefinder.

Also let

$$r_{i-1,j} = (1 + \alpha_{i-1,j})r_{i,j} \tag{17}$$

where $\alpha_{i-1,j}$ indicates the fractional change in true range at point (i-1,j) with respect to point (i,j). Similar expressions are defined for points (i+1,j), (i,j-1), and (i,j+1), with corresponding $\alpha_{i+1,j}$, $\alpha_{i,j-1}$, and $\alpha_{i,j+1}$.

From equations (16) and (17) one can write

$$z_{i-1,j} = (1 + \alpha_{i-1,j})r_{i,j} + v_{i-1,j} \tag{18}$$

It follows that the measurements $z_{i+1,j}$, $z_{i,j-1}$, and $z_{i,j+1}$ can also be expressed in terms of $r_{i,j}$ and the associated noise terms.

For the Normalized Laplacian algorithm, using equations (14) and (18),

$$q_{i,j} = 1 - \frac{4r_{i,j} + 4v_{i,j}}{(4+\alpha_{i-1,j}+\alpha_{i+1,j}+\alpha_{i,j-1}+\alpha_{i,j+1})r_{i,j}+(v_{i-1,j}+v_{i+1,j}+v_{i,j-1}+v_{i,j+1})}$$

Dividing numerator and denominator of the fraction by $4r_{i,j}$:

$$q_{i,j} = 1 - \frac{1 + \left(\frac{v_{i,j}}{r_{i,j}}\right)}{1 + \frac{1}{4}(\alpha_{i-1,j} + \alpha_{i+1,j} + \alpha_{i,j-1} + \alpha_{i,j+1}) + \frac{1}{4}\left(\frac{v_{i-1,j}}{r_{i,j}} + \frac{v_{i+1,j}}{r_{i,j}} + \frac{v_{i,j-1}}{r_{i,j}} + \frac{v_{i,j+1}}{r_{i,j}}\right)} \tag{19}$$

In order to investigate the threshold requirements of $q_{i,j}$, let us assume there is no noise, i.e., $v_{i,j} = 0$ for all i and j. Then, from equation (19),

$$q^*_{i,j} = 1 - \frac{1}{1 + \frac{1}{4}(\alpha_{i-1,j} + \alpha_{i+1,j} + \alpha_{i,j-1} + \alpha_{i,j+1})} \tag{20}$$

The fraction term above can be expanded in a geometric series, with the higher order terms being dropped since the alpha values are all very small. This results in

$$q^*_{i,j} \simeq 1 - \left[1 - \frac{1}{4}(\alpha_{i-1,j} + \alpha_{i+1,j} + \alpha_{i,j-1} + \alpha_{i,j+1})\right]$$

$$= \frac{1}{4}(\alpha_{i-1,j} + \alpha_{i+1,j} + \alpha_{i,j-1} + \alpha_{i,j+1}) \tag{21}$$

In this form, equation (21) can be used to select edge detection threshold values for the Normalized Laplacian Algorithm, given the type of discontinuity to be enhanced. Demonstration of its usage will be given in an example at the end of this section.

Returning to equation (19), the effects of noise can be studied by setting all $\alpha \simeq 0$, so that the laser scans five points nearly equidistant from itself (the inside surface of a sphere, with the laser at the center, may be imagined). Then,

$$q^{\neq}_{i,j} = 1 - \frac{1 + \left(\frac{v_{i,j}}{r_{i,j}}\right)}{1 + \frac{1}{4}\left(\frac{v_{i-1,j}}{r_{i,j}} + \frac{v_{i+1,j}}{r_{i,j}} + \frac{v_{i,j-1}}{r_{i,j}} + \frac{v_{i,j+1}}{r_{i,j}}\right)} \qquad (22)$$

Expanding the fractional term in a geometric series as before

$$q^{\neq}_{i,j} \simeq 1 - \left(1 + \frac{v_{i,j}}{r_{i,j}}\right)\left[1 - \frac{1}{4}\left(\frac{v_{i-1,j}}{r_{i,j}} + \frac{v_{i+1,j}}{r_{i,j}} + \frac{v_{i,j-1}}{r_{i,j}} + \frac{v_{i,j+1}}{r_{i,j}}\right)\right] \qquad (23)$$

Multiplying this out, and dropping higher order powers of the noise terms (which are small),

$$q^{\neq}_{i,j} \simeq -\frac{v_{i,j}}{r_{i,j}} + \frac{1}{4}\left(\frac{v_{i-1,j}}{r_{i,j}} + \frac{v_{i+1,j}}{r_{i,j}} + \frac{v_{i,j-1}}{r_{i,j}} + \frac{v_{i,j+1}}{r_{i,j}}\right) \qquad (24)$$

A single quantity which is a useful measure of the effects of all five noise terms is the variance of $q^{\neq}_{i,j}$, which is defined by

$$\mathrm{var}(q^{\neq}_{i,j}) = E\left\{(q^{\neq}_{i,j} - m)^2\right\} \qquad (25)$$

where $m = E\left\{q^{\neq}_{i,j}\right\}$ = the mean value of $q^{\neq}_{i,j}$

Assuming that the noise v associated with each measurement is independent (so that the variance of the sum equals the sum of the variances), zero mean (so that each m = 0), and has the same standard deviation σ, the variance of $q^{\neq}_{i,j}$ is:

$$\mathrm{var}(q^{+}_{i,j}) = \frac{\sigma^2}{r^2_{i,j}} + 4\left(\frac{\sigma^2}{16 r^2_{i,j}}\right) = \frac{5\,\sigma^2}{4 r^2_{i,j}} \qquad (26)$$

Equation (26) can be used to determine how large a standard deviation may be tolerated without adverse effect on the reliability of the edge detection algorithm. Refer to the example at the end of this section.

The same type of analysis can be performed for the Four Directional Ratio algorithm. Utilizing equation (18), and examining the first term of equation (15),

$$\left(\frac{z_{i-1,j}}{z_{i,j}}\right)^n = \left[\frac{(1 + \alpha_{i-1,j})\, r_{i,j} + v_{i-1,j}}{r_{i,j} + v_{i,j}}\right]^n \tag{27}$$

Dividing numerator and denominator by $r_{i,j}$,

$$\left(\frac{z_{i-1,j}}{z_{i,j}}\right)^n = \left[\frac{1 + \alpha_{i-1,j} + (v_{i-1,j}/r_{i,j})}{1 + (v_{i,j}/r_{i,j})}\right]^n \tag{28}$$

For the case of no noise, i.e., all $v_{i,j} = 0$, equation (28) becomes,

$$\left(\frac{z_{i-1,j}}{z_{i,j}}\right)^{n*} = (1 + \alpha_{i-1,j})^n \tag{29}$$

And neglecting the higher order terms of the polynomial expansion, since α is small,

$$\left(\frac{z_{i-1,j}}{z_{i,j}}\right)^{n*} \simeq 1 + n\,\alpha_{i-1,j} \tag{30}$$

If the same manipulations are performed on the other terms of equation (15), then an expression for the entire algorithm in the absence of noise is approximately,

$$s^*_{i,j} = 1 + \frac{n}{4}(\alpha_{i-1,j} + \alpha_{i+1,j} + \alpha_{i,j-1} + \alpha_{i,j+1}) \tag{31}$$

This equation is analagous to equation (21).

Returning to equation (28), if only noise is being considered, so that all $\alpha \simeq 0$, then

$$\left(\frac{z_{i-1,j}}{z_{i,j}}\right)^{n*} = \frac{(1 + v_{i-1,j}/r_{i,j})^n}{(1 + v_{i,j}/r_{i,j})^n} \tag{32}$$

The numerator of this expression can be written as a polynomial expansion, and the denominator as a geometric power series. Neglecting higher order terms, we are left with,

$$\left(\frac{z_{i-1,j}}{z_{i,j}}\right)^{n\neq} \simeq (1 + n\, v_{i-1,j}/r_{i,j})(1 - n\, v_{i,j}/r_{i,j})$$

$$= \left(1 + n\,\frac{v_{i-1,j}}{r_{i,j}} - n\,\frac{v_{i,j}}{r_{i,j}} - n^2\,\frac{v_{i-1,j}}{r_{i,j}}\,\frac{v_{i,j}}{r_{i,j}}\right) \qquad (33)$$

Extending this result to all terms of equation (15),

$$s^{\neq}_{i,j} = 1 + \frac{n}{4}\left(\frac{v_{i-1,j}}{r_{i,j}} + \frac{v_{i+1,j}}{r_{i,j}} + \frac{v_{i,j-1}}{r_{i,j}} + \frac{v_{i,j+1}}{r_{i,j}}\right) - n\,\frac{v_{i,j}}{r_{i,j}}$$

$$- \frac{n^2}{4}\left(\frac{v_{i,j}}{r_{i,j}}\right)\left(\frac{v_{i-1,j}}{r_{i,j}} + \frac{v_{i+1,j}}{r_{i,j}} + \frac{v_{i,j-1}}{r_{i,j}} + \frac{v_{i,j+1}}{r_{i.j}}\right) \qquad (34)$$

And dropping the products of noise terms,

$$s^{\neq}_{i,j} = 1 + \frac{n}{4}\left(\frac{v_{i-1,j}}{r_{i,j}} + \frac{v_{i+1,j}}{r_{i,j}} + \frac{v_{i,j-1}}{r_{i,j}} + \frac{v_{i,j+1}}{r_{i,j}}\right) - n\,\frac{v_{i,j}}{r_{i,j}} \qquad (35)$$

Under the assumption of independent, zero mean noise with standard deviation σ, an expression for the variance of $s^{\neq}_{i,j}$ follows as before,

$$\mathrm{var}(s^{\neq}_{i,j}) = 4\left(\frac{n^2\sigma^2}{16r^2_{i,j}}\right) + n^2\,\frac{\sigma^2}{r^2_{i,j}} = \frac{5n^2\sigma^2}{4r^2_{i,j}} \qquad (36)$$

This equation is analagous to equation (26).

The foregoing analysis gives the means of choosing the proper thresholds, given the values of α. For example, if two of the outer points (i-1,j) and (i,j-1) lie outside the obstacle and the other three points, including the central point (i,j), lie on the obstacle, then one

may assume that $\alpha_{i-1,j}, \alpha_{i,j-1} > 0$ and $\alpha_{i+1,j}, \alpha_{i,j+1} \simeq 0$.

To generate some typical numerical results, let

$$\alpha_{i-1,j} \simeq \alpha_{i,j-1} \simeq 0.04 \tag{37}$$

Then for the Normalized Laplacian algorithm, from equation (21),

$$q^*_{i,j} = \frac{1}{4}(0.04 + 0 + 0.04 + 0) = 0.02 \tag{38}$$

Thus, the threshold may be set just below 0.02 if the point in consideration is to be recognized as lying just inside the edge of the obstacle, i.e.

$$T_{qi} \simeq 0.019 \tag{39}$$

Similarly, if three of the outer points, including the central point (i,j) lie outside the obstacle, and the other two points (i+1,j) and (i,j+1) lie on the obstacle, then we might take,

$$\alpha_{i-1,j} \simeq \alpha_{i,j-1} \simeq 0 \tag{40}$$

$$\alpha_{i+1,j} \simeq \alpha_{i,j+1} \simeq -0.04 \tag{41}$$

Equation (21) now becomes,

$$q^*_{i,j} = \frac{1}{4}(0 + (-0.04) + 0 + (-0.04)) = -0.02 \tag{42}$$

so that the threshold may be set near this number if the point in consideration is to be recognized as lying just outside the edge of the obstacle, i.e.,

$$T_{qo} \simeq -0.019 \tag{43}$$

In the case of the Four Directional Ratio algorithm, using the same alpha values, we have from equation (31),

$$s^*_{i,j} = 1 + \frac{n}{4}(0.04 + 0 + 0.04 + 0) = 1 + n(0.02) \qquad (44)$$

for an inside edge

$$s^*_{i,j} = 1 + \frac{n}{4}(0 + (-0.04) + 0 + (-0.04) = 1 - n(0.02) \qquad (45)$$

for an outside edge

Notice that by increasing n we can amplify the apparent threshold values, and that for n = 1 the thresholds are the same (within a constant) as those for the Normalized Laplacian algorithm, i.e.

$$s^*_{i,j} = q^*_{i,j} + 1 \quad \text{for } n = 1 \qquad (46)$$

Computer simulations were run using n = 1 and n = 2, the first case being used as a check for agreement to the Normalized Laplacian algorithm results and the second case investigating the possible improvements in performance obtainable by increasing n.

The two sets of thresholds are therefore,

for n = 1 $T_{si} \simeq 1.019$ for an inside edge (47)

$T_{so} \simeq .981$ for an outside edge (48)

for n = 2 $T_{si} \simeq 1.038$ for an inside edge (49)

$T_{so} \simeq .962$ for an outside edge (50)

The true values of alpha may be practicably obtained from a physical model of obstacles and terrains that may presumably be encountered on Mars. By examining different types of configurations in simulations, we may predetermine the specific values of alpha to use for thresholding in each case.

The variances given in equations (26) and (36) afford us an

indication of how large a measurement noise may be accommodated by the algorithms. Suppose it is desired that the threshold lies outside the 1σ limit of the variations in the algorithms. For the Normalized Laplacian algorithm, from equations (26) and (39),

$$\sqrt{\frac{5\sigma^2}{4r^2_{i,j}}} \leq 0.019$$

or
$$\sigma \leq \frac{(2)(0.019)}{\sqrt{5}} \; r_{i,j}$$

$$\sigma \leq 0.017 \; r_{i,j} \tag{51}$$

With this value of σ we will have approximately 70% certainty regarding the accuracy of the detections. Obviously at longer ranges, higher measurement noise may be allowed.

For the Four Directional Ratio algorithm, keeping in mind that we are comparing the statistics of noise to the variations in threshold, we have from equations (36) and (44),

$$\sqrt{\frac{5n^2\sigma^2}{4r^2_{i,j}}} \leq n(0.019)$$

or,
$$\sigma \leq \frac{(2)(0.019)}{\sqrt{5}} \; r_{i,j}$$

$$\sigma \leq 0.017 \; r_{i,j} \tag{52}$$

This is the same bound on σ that was found for the Normalized Laplacian algorithm. Since both the threshold values and the noise effects are increasing linearly with n according to this analysis, there is no

apparent merit to be derived from changing n in this algorithm, i.e., no improvement in the quality of the enhanced edge. This conclusion will be checked in the computer simulations which follow.

4. COMPUTER SIMULATION PROGRAM

Now that a mathematical model of the edge detection problem has been established, and analytical procedures proposed for implementing the scheme, a computer program is needed to carry out the simulation. Such a program was developed for this purpose; a flowchart of the steps involved appears in Figure 3.

Several features of the program should be noted:

1) In generating range values which lay on the boulder, it was necessary to use the double precision option on the IBM 360-50 computer. The reason for this is seen by examining equation (11) closely. The trionometric functions of β and θ in this expression are calculated by means of a Taylor series in the computer. Since the angles involved are so small, and the differencesbetween the angles are at least an order of magnitude smaller still (approaching $0.1^{\circ} \simeq 0.002$ radians), it is desireable to have the greatest possible accuracy in determining the sines and cosines. It was found experimentally that single precision sometimes led to significant errors in these range values, which is unacceptable since the errors in the geometric range data should be at least an order of magnitude smaller than the standard deviation of the Gaussian noise added to the data in order for the noise to be physically meaningful. Thus, double precision was needed to achieve range values accurate to within $\pm$ .005 m at least. Longer CPu times were required for double precision in the simulation; however, on the actual Mars Rover the range readings will be measured rather than calculated, so that the additional computer time for this step will not be a factor in the on-board computer.

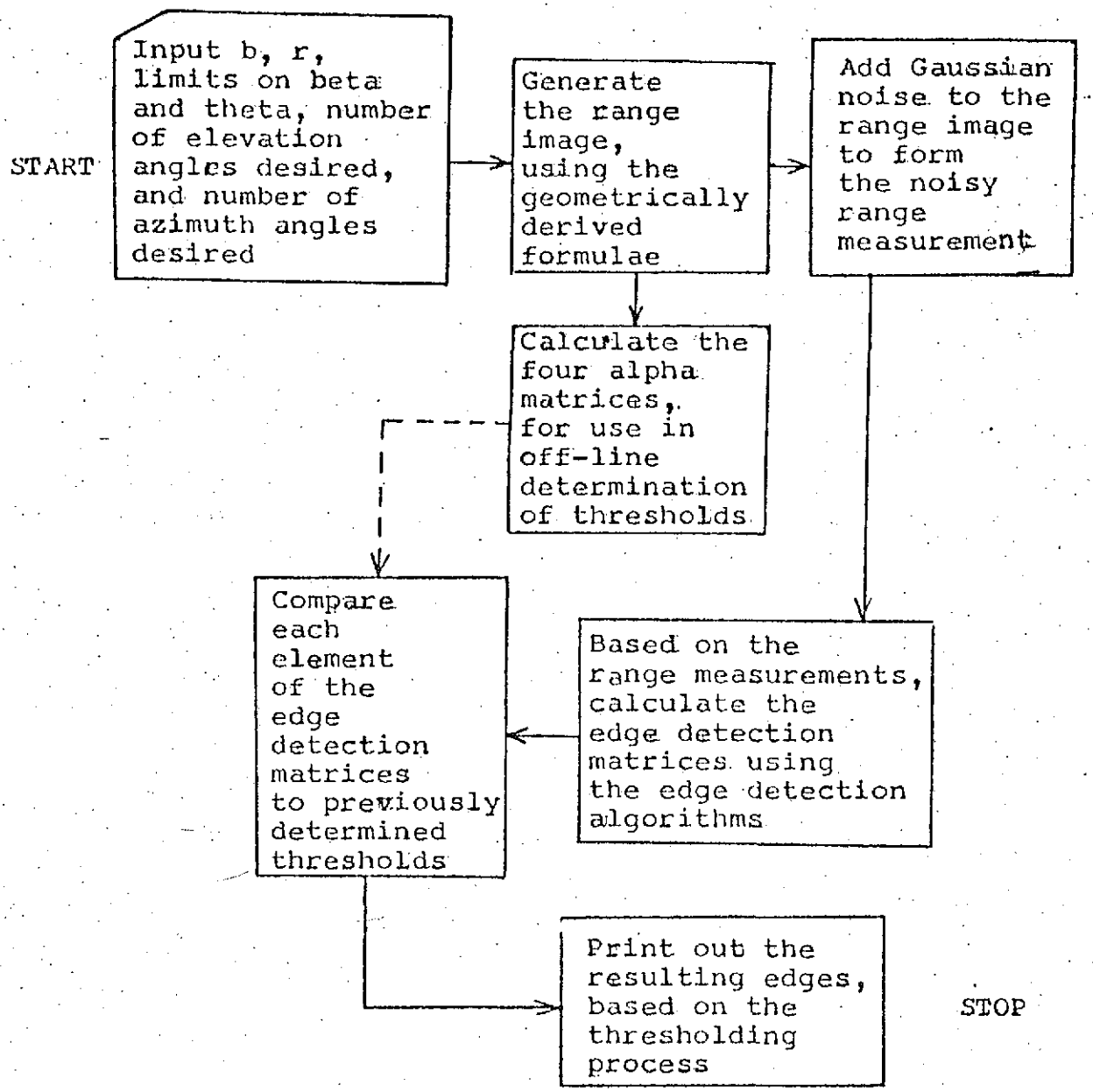

FIGURE 3

Flowchart of Computer Simulation Main Program

2) Two of the variables in this program are the number of different elevation angles and the number of different aximuth angles to be scanned. The product of these two values equals the total number of points contained in the measurement matrix, which, along with the angle limits, is a measure of the "resolution" of the range image. As discussed previously, it has been assumed that each range measurement by the Rover will take approximately 1 msec to complete. In the simulations which follow there are a total of 525 points in the range image (25 separate elevation angles and 21 separate azimuth angles). Therefore, under nominal conditions, the Rover would require approximately 1/2 second to record all these range values, in which time it would travel approximately 1/2 meter. The effect of this motion on the algorithms has been neglected, which at first may seem to be rather a severe assumption. On the other hand, when operating on the range values for the purpose of edge detection, only five neighboring points in the measurement matrix are compared at any one time. If the laser beam scans the terrain ahead in a W-shaped pattern, then these five measurements will be taken within a few milliseconds of each other. In this light, it was deemed acceptable to neglect the vehicle's motion; it will be left to future research efforts to investigate its effect.

3) The limits on the angles also warrant some discussion. For the most part these limits were chosen with the a priori knowledge of the size and location of the obstacle, so as to maximize the information received for edge detection. This is a very contrived situation, and illustrated part of the complex problem of scanning scheme determination, which will be examined in Section 6.

4) Thresholds used in each algorithm were chosen off-line, once the alpha matrices for the simulated terrain were calculated and printed out by the computer. This is considered to be a valid procedure, since it is not now expected that the Rover will be capable of adaptively choosing thresholds for edge detection, but rather will use pre-stored values (based on simulations much like this one) as a basis for its decisions.

5. SIMULATION RESULTS FOR BOULDERS

5.1 The Boulder at 30 Meters

The initial computer simulations were conducted for the case of a 1.0 meter radius hemispherical boulder located 30 meters in front of the Rover. These numbers were selected so as to provide a true obstacle that had to be detected and avoided (since physical limitations on the vehicle prohibit it from navigating over a discontinuity of more than about .5 meters under normal conditions) and to place this obstacle at a typical mid-range location at which edge detection by means of range data manipulation becomes most important for path selection decisions.

Figure 4 illustrates the resulting computer-generated range images. The upper matrix represents the geometrically derived, undistorted measurements, and the lower matrix represents these same values when contaminated by zero mean, 5 cm standard deviation, Gaussian noise. Thus, the lower matrix simulates the range values that will be obtained by means of the laser rangefinder on the Rover. In both cases the outline of the boulder has been drawn in its approximate location, to clarify for the reader how the scanning procedure will operate. The exact angles used, and their orientation on the range image, can be determined from the data listed at the top of the page.

As outlined in Section 3.4, four α parameters can be defined for each element of the undistorted range image, and so four α matrices can be found to describe the entire range image. Figures 5 and 6 depict these four matrices, which are used in the off-line determination of threshold values by the procedures discussed. As an example of the

CALCULATED RANGE DATA FOR A HEMISPHERICAL BOULDER (1.00 METER RADIUS) AT A DISTANCE OF 30.00 METERS FROM MARS ROVER

BETA MAX = 6.0 DEGREES BETA MIN = 3.0 DEGREES BETA INCREMENT = .15 DEGREES
THETA MAX = 3.0 DEGREES THETA MIN = -3.0 DEGREES THETA INCREMENT = .30 DEGREES

R(1,1)-----(BETA MIN, THETA MIN)
R(25,1)-----(BETA MAX, THETA MIN)

R(1,21)-----(BETA MIN, THETA MAX)
R(25,21)-----(BETA MAX, THETA MAX)

UNDISTORTED BY NOISE

```
50.00 50.00 50.00 50.00 50.00 50.00 50.00 50.00 50.00 50.00 50.00 50.00 50.00 50.00 50.00 50.00 50.00 50.00 50.00 50.00 50.00
50.00 50.00 50.00 50.00 50.00 50.00 50.00 50.00 50.00 50.00 50.00 50.00 50.00 50.00 50.00 50.00 50.00 50.00 50.00 50.00 50.00
50.00 50.00 50.00 50.00 50.00 50.00 50.00 50.00 50.00 50.00 50.00 50.00 50.00 50.00 50.00 50.00 50.00 50.00 50.00 50.00 50.00
49.88 49.88 49.88 49.88 49.88 49.88 49.88 49.88 49.88 49.88 49.88 49.88 49.88 49.88 49.88 49.88 49.88 49.88 49.88 49.88 49.88
47.75 47.75 47.75 47.75 47.75 47.75 47.75 47.75 47.75 47.75 47.75 47.75 47.75 47.75 47.75 47.75 47.75 47.75 47.75 47.75 47.75
45.88 45.88 45.88 45.88 45.88 45.88 45.88 45.88 45.88 45.88 45.88 45.88 45.88 45.88 45.88 45.88 45.88 45.88 45.88 45.88 45.88
44.13 44.13 44.13 44.13 44.13 44.13 44.13 44.13 44.13 44.13 44.13 44.13 44.13 44.13 44.13 44.13 44.13 44.13 44.13 44.13 44.13
42.50 42.50 42.50 42.50 42.50 42.50 42.50 42.50 42.50 42.50 42.50 42.50 42.50 42.50 42.50 42.50 42.50 42.50 42.50 42.50 42.50
40.94 40.94 40.94 40.94 40.94 40.94 40.94 40.94 40.94 40.94 40.94 40.94 40.94 40.94 40.94 40.94 40.94 40.94 40.94 40.94 40.94
39.50 39.50 39.50 39.50 39.50 39.50 39.50 39.50 39.50 39.50 39.50 39.50 39.50 39.50 39.50 39.50 39.50 39.50 39.50 39.50 39.50
38.25 38.25 38.25 38.25 38.25 38.25 38.25 38.25 38.25 38.25 38.25 38.25 38.25 38.25 38.25 38.25 38.25 38.25 38.25 38.25 38.25
37.06 37.06 37.06 37.06 37.06 37.06 37.06 37.06 37.06 37.06 37.06 37.06 37.06 37.06 37.06 37.06 37.06 37.06 37.06 37.06 37.06
35.88 35.88 35.88 35.88 35.88 35.88 35.88 35.88 35.88 35.88 35.88 35.88 35.88 35.88 35.88 35.88 35.88 35.88 35.88 35.88 35.88
34.75 34.75 34.75 34.75 34.75 34.75 34.75 34.75 34.75 34.75 34.75 34.75 34.75 34.75 34.75 34.75 34.75 34.75 34.75 34.75 34.75
33.75 33.75 33.75 33.75 33.75 33.75 33.75 33.75 33.75 33.75 33.75 33.75 33.75 33.75 33.75 33.75 33.75 33.75 33.75 33.75 33.75
32.75 32.75 32.75 32.75 32.75 32.75 32.75 32.75 32.75 32.75 32.75 32.75 32.75 32.75 32.75 32.75 32.75 32.75 32.75 32.75 32.75
31.88 31.88 31.88 31.88 31.88 31.88 31.88 31.88 31.88 31.88 31.88 31.88 31.88 31.88 31.88 31.88 31.88 31.88 31.88 31.88 31.88
31.06 31.06 31.06 31.06 31.06 31.06 31.06 31.06 31.06 31.06 31.06 31.06 31.06 31.06 31.06 31.06 31.06 31.06 31.06 31.06 31.06
30.25 30.25 30.25 30.25 30.25 30.25 30.25 30.25 30.25 30.25 30.25 30.25 30.25 30.25 30.25 30.25 30.25 30.25 30.25 30.25 30.25
29.44 29.44 29.44 29.44 29.44 29.44 29.44 29.44 29.44 29.44 29.44 29.44 29.44 29.44 29.44 29.44 29.44 29.44 29.44 29.44 29.44
28.69 28.69 28.69 28.69 28.69 28.69 28.69 28.69 28.69 28.69 28.69 28.69 28.69 28.69 28.69 28.69 28.69 28.69 28.69 28.69 28.69
28.03 28.03 28.03 28.03 28.03 28.03 28.03 28.03 28.03 28.03 28.03 28.03 28.03 28.03 28.03 28.03 28.03 28.03 28.03 28.03 28.03
27.38 27.38 27.38 27.38 27.38 27.38 27.38 27.38 27.38 27.38 27.38 27.38 27.38 27.38 27.38 27.38 27.38 27.38 27.38 27.38 27.38
26.69 26.69 26.69 26.69 26.69 26.69 26.69 26.69 26.69 26.69 26.69 26.69 26.69 26.69 26.69 26.69 26.69 26.69 26.69 26.69 26.69
26.13 26.13 26.13 26.13 26.13 26.13 26.13 26.13 26.13 26.13 26.13 26.13 26.13 26.13 26.13 26.13 26.13 26.13 26.13 26.13 26.13
```

CONTAMINATED BY ZERO MEAN, .05 METER STANDARD DEVIATION, GAUSSIAN NOISE

```
49.97 50.00 50.04 50.01 49.96 49.99 50.06 50.01 49.97 50.05 49.99 50.04 50.10 49.97 50.03 49.99 50.11 50.02 50.10 50.02 50.01
49.96 50.00 50.07 49.78 49.94 49.97 49.96 49.93 49.94 50.05 50.01 50.01 50.06 49.94 50.10 50.00 50.04 50.02 50.06 49.98 50.11
50.03 50.04 50.13 50.01 49.92 50.02 50.01 49.97 49.96 49.93 50.07 49.91 50.07 49.97 50.05 49.93 50.03 50.01 50.03 49.99 50.03
49.87 49.92 49.90 49.89 49.77 49.88 49.89 49.95 49.87 49.94 49.87 49.91 49.94 49.84 49.88 49.93 49.84 49.78 49.99 49.88 49.86
47.80 47.76 47.77 47.72 47.77 47.82 47.84 47.84 47.78 47.73 47.74 47.83 47.97 47.81 47.86 47.73 47.78 47.75 47.78 47.81 47.70
45.99 45.86 45.89 45.87 45.94 45.90 45.88 45.79 45.93 45.89 45.95 45.91 45.87 45.93 45.95 45.81 45.97 45.90 45.84 45.77 45.87
44.13 44.11 44.12 44.12 44.12 44.16 44.12 44.09 44.15 44.11 44.10 44.06 44.11 44.10 44.06 44.17 44.09 44.10 44.12 44.13
42.51 42.49 42.50 42.47 42.51 42.41 42.51 42.44 42.42 42.60 42.69 42.72 42.51 42.44 42.47 42.47 42.58 42.44 42.53 42.51
40.96 40.91 40.96 41.05 40.88 40.96 41.03 40.86 40.93 40.93 40.94 40.87 40.85 40.97 40.90 40.86 40.90 40.94 40.88 40.89
39.44 39.49 39.55 39.47 39.49 39.98 39.84 39.96 39.89 39.82 39.87 39.87 39.98 39.88 39.84 39.52 39.52 39.49 39.47 39.53 39.41
38.21 38.18 38.27 38.23 38.26 38.27 38.24 38.24 38.42 38.34 38.36 38.38 38.45 38.47 38.76 38.31 38.27 38.27 38.30 38.25 38.35
37.07 37.11 37.11 37.03 37.06 37.23 37.13 37.53 37.39 37.35 37.36 37.36 37.19 37.45 37.48 37.64 37.54 37.06 36.98 37.06 36.96 37.37
35.87 35.97 35.88 35.91 35.89 35.78 35.98 35.83 35.83 35.87 35.95 35.89 35.89 35.89 35.89 35.83 35.82 35.82 35.93 35.84
34.71 34.75 34.72 34.75 34.68 34.89 34.98 34.80 34.86 34.86 34.86 34.84 34.82 34.85 34.90 34.93 34.72 34.77 34.78 34.73 34.79
33.77 33.87 33.72 33.78 33.75 34.07 33.97 33.95 33.96 33.85 33.86 33.87 33.81 33.86 33.87 33.89 33.77 33.78 33.66 33.79 33.72
32.69 32.68 32.79 32.74 32.77 32.93 32.91 32.89 32.83 32.87 32.84 32.84 32.84 32.85 32.89 32.91 32.76 32.68 32.80 32.80
31.79 31.83 31.87 31.83 31.89 31.89 31.97 31.92 31.84 31.84 31.83 31.83 31.81 31.87 31.86 31.91 31.84 31.89 31.81 31.80
31.11 31.07 31.03 31.08 31.04 31.24 31.23 31.43 31.20 31.15 31.21 31.16 31.16 31.25 31.25 31.32 31.56 31.60 31.11 31.01 31.07 31.01
30.25 30.17 30.25 30.17 30.23 30.43 30.42 30.33 30.18 30.15 30.21 30.17 30.17 30.17 30.23 30.21 30.41 30.41 30.14 30.20 30.31 30.22
29.51 29.49 29.47 29.47 29.44 29.64 29.64 29.79 29.64 29.77 29.71 29.69 29.76 29.70 29.77 29.72 29.67 29.63 29.32 29.48 29.45 29.49
28.72 28.77 28.68 28.68 28.74 28.77 28.72 28.79 28.82 28.87 28.83 28.89 28.72 28.68 28.87 28.61 28.75 28.69 28.79 28.60 28.75
27.94 27.99 28.00 28.05 27.97 27.95 28.07 28.03 28.00 27.95 28.03 28.02 28.01 28.12 28.00 28.05 28.08 28.05 28.09 27.98 27.97
27.38 27.33 27.34 27.42 27.34 27.28 27.36 27.34 27.47 27.36 27.37 27.41 27.41 27.31 27.31 27.36 27.39 27.35 27.28 27.39 27.48
26.71 26.69 26.73 26.74 26.70 26.80 26.85 26.86 26.88 26.73 26.79 26.88 26.89 26.70 26.64 26.70 26.69 26.71 26.62 26.68 26.71
26.24 26.12 26.12 26.08 26.20 26.00 26.10 26.12 26.14 26.13 26.21 26.16 26.04 26.15 26.07 26.28 26.15 26.10 26.12 26.13 26.12
```

FIGURE 4

The Range Image for a Boulder at 30 m

approximate thresholds to be expected in cases like this one, and to show agreement with the analysis given, a threshold of 1.02 was used in the Four Directional Ratio algorithm (with n = 1) to pick out the points close to the inside edge of the boulder, and a value of .96 was used to pick out the points close to the outside edge.

Applying the two algorithms (the Four Directional Ratio with n = 2 and the Normalized Laplacian) to each of the measurements contained in the noisy range image (except for the extreme top and bottom rows, and left and right columns, since none of these measurements has all four of the associated neighboring points defined in the algorithms) yields the two edge detection matrices pictured in Figure 7. It should be noted that the range measurement noise being simulated has virtually no effect on the elements of these matrices, since from equation (51), for $r_{i,j} \simeq 30$, we have that σ allowable $\simeq .017\, r_{i,j} \simeq .51$, whereas the standard deviation of noise used is only .05. This indicates that, with the accuracy of the laser rangefinder as assumed, the edge detection scheme is quite insensitive to noise, which is a very encouraging conclusion for this aspect of performance.

Finally, in Figure 8, we see the outlines of the boulder after the thresholding operation has been applied to the previous matrices. The outcome obtained by means of the Four Directional Ratio algorithm with n = 1 has been suppressed in this and all subsequent figures to avoid redundancy, since the results are nearly identical to those of the Normalized Laplacian algorithm, as explained in Section 3.4 and proven experimentally. In these pictures an "x" re-

MATRIX OF ALPHA(I-1,J) VALUES

I = 2 TO 25 / J = 1 TO 21

MATRIX OF ALPHA(I+1,J) VALUES

I = 1 TO 24 / J = 1 TO 21

FIGURE 5

Two of the α Matrices for a Boulder at 30 m

MATRIX OF ALPHA(I,J-1) VALUES

I = 1 TO 25 / J = 2 TO 21

MATRIX OF ALPHA(I,J+1) VALUES

I = 1 TO 25 / J = 1 TO 20

FIGURE 6

Two of the α Matrices for a Boulder at 30 m

FOUR DIRECTIONAL RATIO EDGE DETECTION SCHEME, WITH N=2

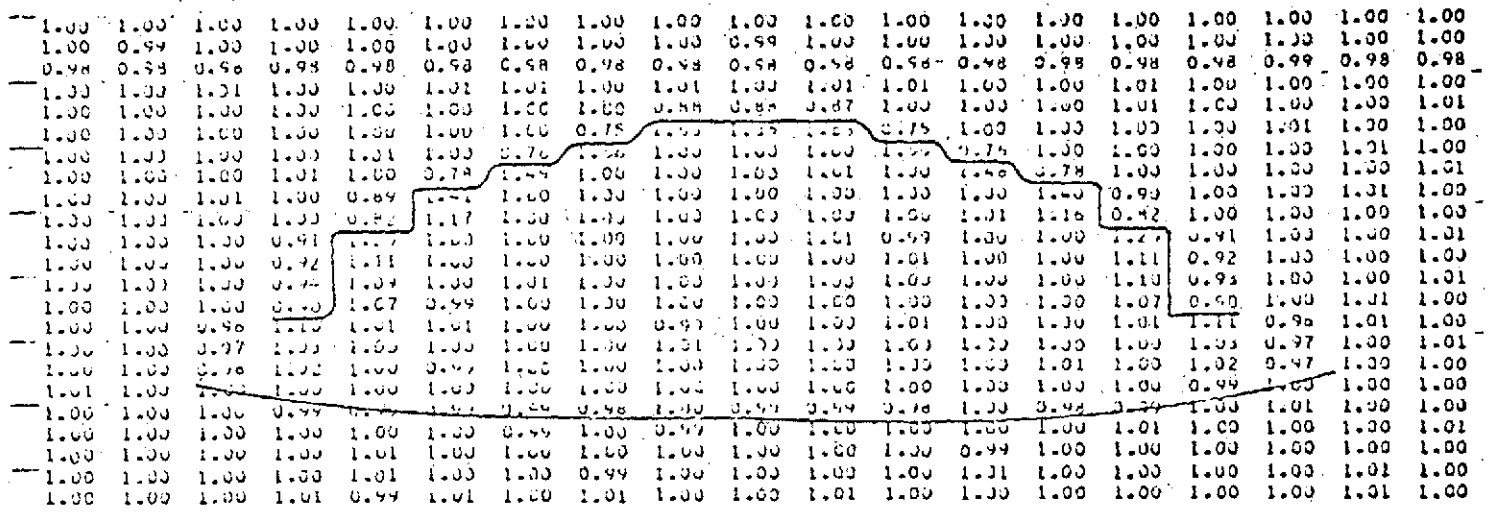

NORMALIZED LAPLACIAN EDGE DETECTION SCHEME

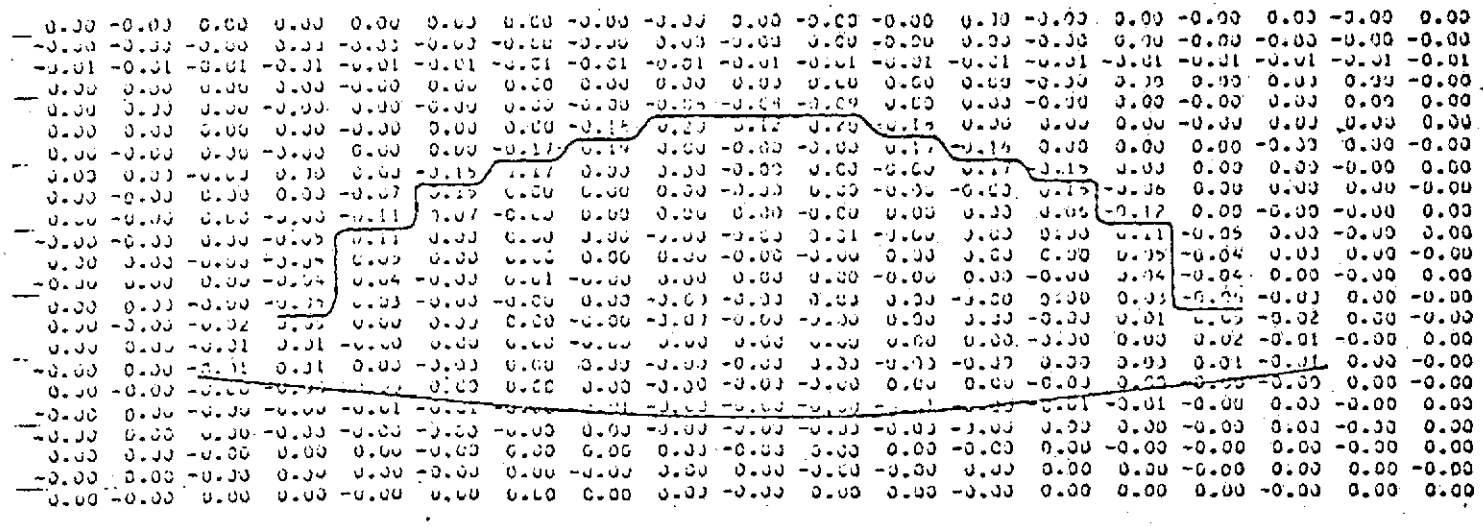

FIGURE 7

The Edge Detection Matrices for a Boulder at 30 m

EDGE ENHANCEMENT BASED ON FOUR DIRECTIONAL RATIO (N=2)

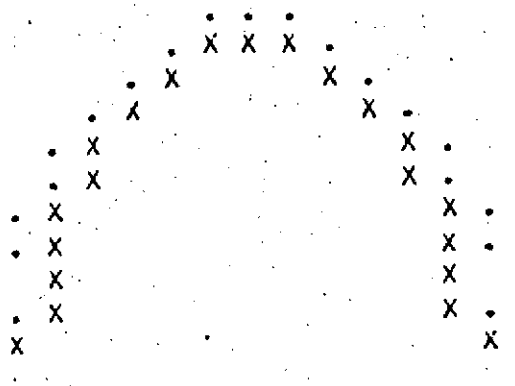

EDGE ENHANCEMENT BASED ON NORMALIZED HAMILTONIAN

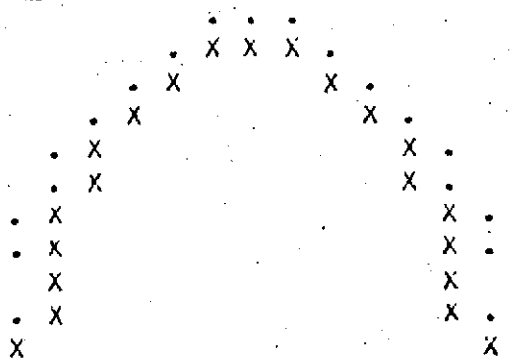

FIGURE 8

Outlines of the Boulder at 30 m

presents a detected inside edge point (one that lies close to the edge and is on the obstacle) and a "." represents a detected outside edge point (one that lies close to the edge, as seen from the laser, and is on the terrain). The true edge, therefore, lies between the sets of these two "near edge" points. As is evident, by proper choice of thresholds both algorithms yield pictures which are quite good representations of the boulder's edge. It was expected that the Four Directional Ratio algorithm with $n > 1$ would not result in a more complete edge than the Normalized Laplacian algorithm, based on the argument at the end of Section 3.4, and a trend of this type was noted in the simulations. More conclusive evidence could have been obtained if n was increased beyond the value of 2, but no such tests were run. This point must ultimately be investigated and resolved before a final algorithm choice can be implemented.

Due to the nature of the algorithms, the fact that the bottom edge of the boulder is not detected is a characteristic outcome and should be expected. In other words, since the edge detection scheme is based on the search of neighboring range elements for sharp changes in their values in order to locate an edge, there will be no such indication if the adjacent measurements are approximately the same (as they are for points on the same terrain feature and also for points near the bottom edge). A different type of algorithm is therefore needed for this special case. Further discussion on this subject can be found in Section 5.3.

5.2 Other Mid-Range Boulders

Since the laser rangefinder will be required to provide information about the terrain in the entire mid-range field (approximately 3 to 30 meters in front of the Rover), the edge detection scheme was tested for boulders located at distances other than 30 meters. It was decided that boulders located at 10 m, 20 m, and 40 m, in addition to the one located at 30 m, would be suitable for determination of the capabilities of the edge detection algorithms.

The range images and boulder outlines of these three additional cases appear in Figures 9 through 14. By proper choice of scanning angle limits and threshold values, all outcomes are equally satisfactory (except for the continued lack of bottom edges). Therefore, this type of edge detection scheme is considered a viable procedure for recognition of mid-range positive obstacles.

5.3 The Bottom Edge

As it has been pointed out, all the boulder edge outlines seen thus far have been without a bottom edge, due to the nature of the enhancement algorithms. In order to determine the size of an obstacle, and so how much of a potential hindrance to the progress of the Rover that it represents, it is considered important to develop an alternate scheme to detect this bottom edge based on the laser's range measurements.

The first attempt at a solution to this problem was founded on the observation (which can be easily proven geometrically) that range values measured to the bottom edge itself form a set of local

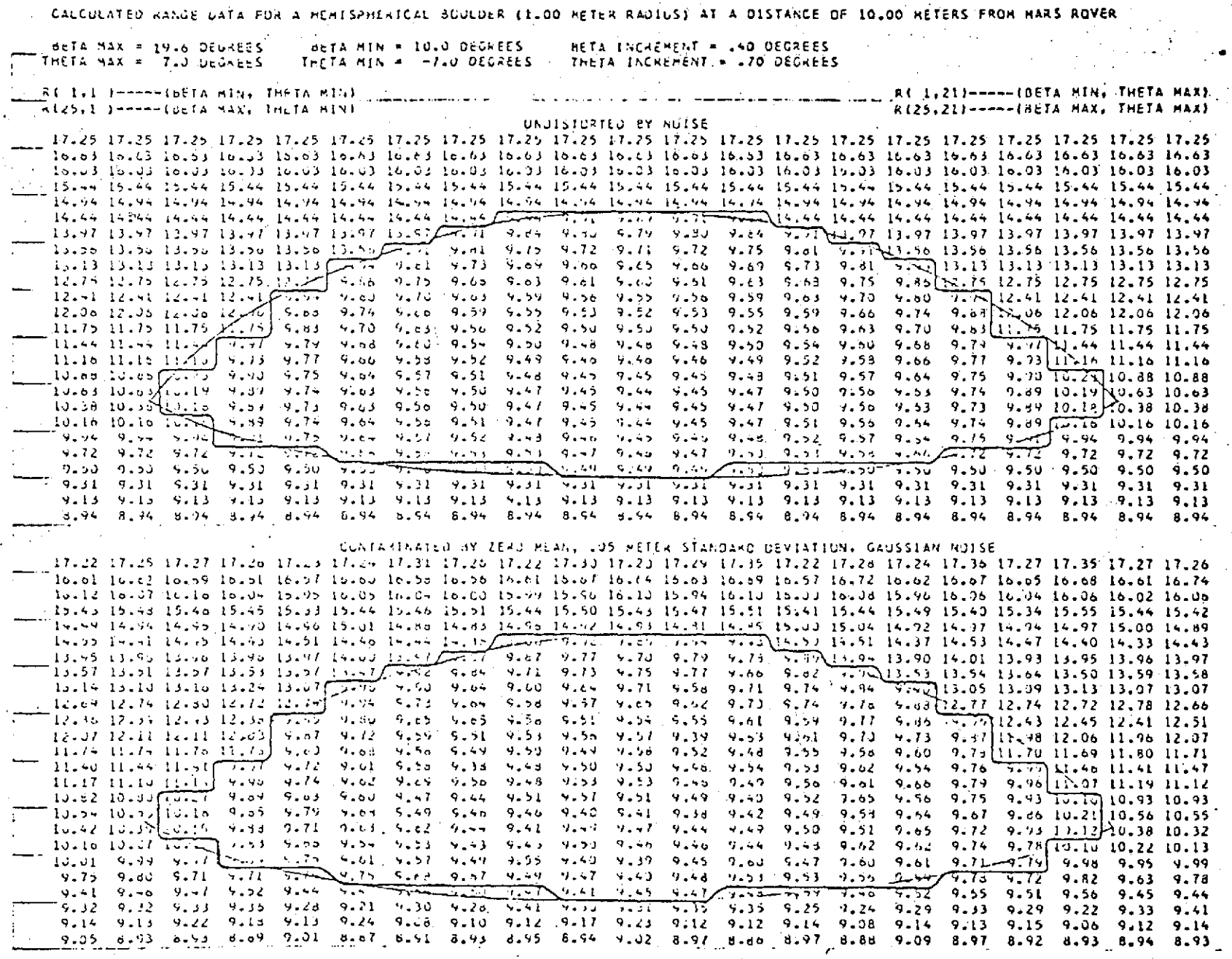

FIGURE 9

The Range Image for a Boulder at 10 m

EDGE ENHANCEMENT BASED ON FOUR DIRECTIONAL RATIO (N=2)

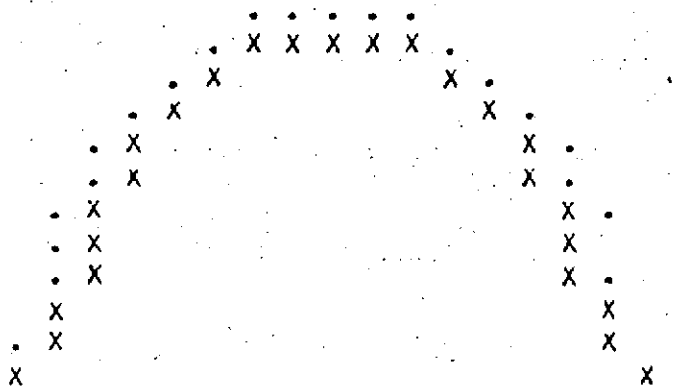

EDGE ENHANCEMENT BASED ON NORMALIZED HAMILTONIAN

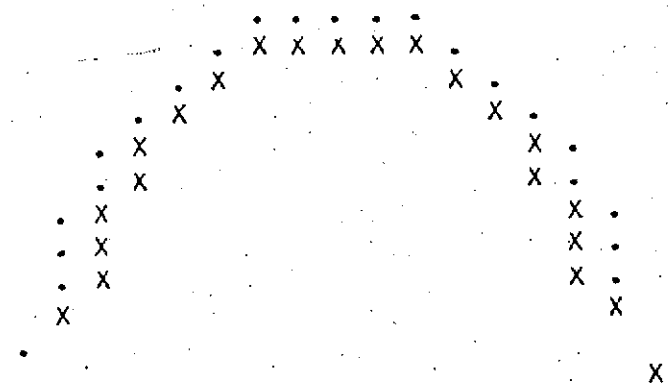

FIGURE 10

Outlines of the Boulder at 10 m

CALCULATED RANGE DATA FOR A HEMISPHERICAL BOULDER (1.00 METER RADIUS) AT A DISTANCE OF 20.00 METERS FROM MARS ROVER

BETA MAX = 9.0 DEGREES BETA MIN = .5.0 DEGREES BETA INCREMENT = .20 DEGREES
THETA MAX = 4.0 DEGREES THETA MIN = -4.0 DEGREES THETA INCREMENT = .40 DEGREES

R(1,1)-----(BETA MIN, THETA MIN)
R(25,1)-----(BETA MAX, THETA MIN)
R(1,21)-----(BETA MIN, THETA MAX)
R(25,21)-----(BETA MAX, THETA MAX)

UNDISTORTED BY NOISE

34.38	34.38	34.38	34.38	34.38	34.38	34.38	34.38	34.38	34.38	34.38	34.38	34.38	34.38	34.38	34.38	34.38	34.38	34.38	34.38	34.38	34.38	34.38
33.13	33.13	33.13	33.13	33.13	33.13	33.13	33.13	33.13	33.13	33.13	33.13	33.13	33.13	33.13	33.13	33.13	33.13	33.13	33.13	33.13	33.13	33.13
31.88	31.88	31.88	31.88	31.88	31.88	31.88	31.88	31.88	31.88	31.88	31.88	31.88	31.88	31.88	31.88	31.88	31.88	31.88	31.88	31.88	31.88	31.88
30.75	30.75	30.75	30.75	30.75	30.75	30.75	30.75	30.75	30.75	30.75	30.75	30.75	30.75	30.75	30.75	30.75	30.75	30.75	30.75	30.75	30.75	30.75
29.69	29.69	29.69	29.69	29.69	29.69	29.69	29.69	29.69	29.69	29.69	29.69	29.69	29.69	29.69	29.69	29.69	29.69	29.69	29.69	29.69	29.69	29.69
28.69	28.69	28.69	28.69	28.69	28.69	28.69	28.69	28.69	28.69	28.69	28.69	28.69	28.69	28.69	28.69	28.69	28.69	28.69	28.69	28.69	28.69	28.69
27.75	27.75	27.75	27.75	27.75	27.75	27.75	27.75	27.75	27.75	27.75	27.75	27.75	27.75	27.75	27.75	27.75	27.75	27.75	27.75	27.75	27.75	27.75
26.88	26.88	26.88	26.88	26.88	26.88	26.88	26.88	26.88	26.88	26.88	26.88	26.88	26.88	26.88	26.88	26.88	26.88	26.88	26.88	26.88	26.88	26.88
26.13	26.13	26.13	26.13	26.13	26.13	26.13	26.13	26.13	26.13	26.13	26.13	26.13	26.13	26.13	26.13	26.13	26.13	26.13	26.13	26.13	26.13	26.13
25.38	25.38	25.38	25.38	25.38	25.38	25.38	25.38	25.38	25.38	25.38	25.38	25.38	25.38	25.38	25.38	25.38	25.38	25.38	25.38	25.38	25.38	25.38
24.63	24.63	24.63	24.63	24.63	24.63	24.63	24.63	24.63	24.63	24.63	24.63	24.63	24.63	24.63	24.63	24.63	24.63	24.63	24.63	24.63	24.63	24.63
23.94	23.94	23.94	23.94	23.94	23.94	23.94	23.94	23.94	23.94	23.94	23.94	23.94	23.94	23.94	23.94	23.94	23.94	23.94	23.94	23.94	23.94	23.94
23.31	23.31	23.31	23.31	23.31	23.31	23.31	23.31	23.31	23.31	23.31	23.31	23.31	23.31	23.31	23.31	23.31	23.31	23.31	23.31	23.31	23.31	23.31
22.69	22.69	22.69	22.69	22.69	22.69	22.69	22.69	22.69	22.69	22.69	22.69	22.69	22.69	22.69	22.69	22.69	22.69	22.69	22.69	22.69	22.69	22.69
22.13	22.13	22.13	22.13	22.13	22.13	22.13	22.13	22.13	22.13	22.13	22.13	22.13	22.13	22.13	22.13	22.13	22.13	22.13	22.13	22.13	22.13	22.13
21.56	21.56	21.56	21.56	21.56	21.56	21.56	21.56	21.56	21.56	21.56	21.56	21.56	21.56	21.56	21.56	21.56	21.56	21.56	21.56	21.56	21.56	21.56
21.06	21.06	21.06	21.06	21.06	21.06	21.06	21.06	21.06	21.06	21.06	21.06	21.06	21.06	21.06	21.06	21.06	21.06	21.06	21.06	21.06	21.06	21.06
20.56	20.56	20.56	20.56	20.56	20.56	20.56	20.56	20.56	20.56	20.56	20.56	20.56	20.56	20.56	20.56	20.56	20.56	20.56	20.56	20.56	20.56	20.56
20.06	20.06	20.06	20.06	20.06	20.06	20.06	20.06	20.06	20.06	20.06	20.06	20.06	20.06	20.06	20.06	20.06	20.06	20.06	20.06	20.06	20.06	20.06
19.63	19.63	19.63	19.63	19.63	19.63	19.63	19.63	19.63	19.63	19.63	19.63	19.63	19.63	19.63	19.63	19.63	19.63	19.63	19.63	19.63	19.63	19.63
19.19	19.19	19.19	19.19	19.19	19.19	19.19	19.19	19.19	19.19	19.19	19.19	19.19	19.19	19.19	19.19	19.19	19.19	19.19	19.19	19.19	19.19	19.19
18.75	18.75	18.75	18.75	18.75	18.75	18.75	18.75	18.75	18.75	18.75	18.75	18.75	18.75	18.75	18.75	18.75	18.75	18.75	18.75	18.75	18.75	18.75
18.38	18.38	18.38	18.38	18.38	18.38	18.38	18.38	18.38	18.38	18.38	18.38	18.38	18.38	18.38	18.38	18.38	18.38	18.38	18.38	18.38	18.38	18.38
17.97	17.97	17.97	17.97	17.97	17.97	17.97	17.97	17.97	17.97	17.97	17.97	17.97	17.97	17.97	17.97	17.97	17.97	17.97	17.97	17.97	17.97	17.97
17.63	17.63	17.63	17.63	17.63	17.63	17.63	17.63	17.63	17.63	17.63	17.63	17.63	17.63	17.63	17.63	17.63	17.63	17.63	17.63	17.63	17.63	17.63

CONTAMINATED BY ZERO MEAN, .05 METER STANDARD DEVIATION, GAUSSIAN NOISE

34.35	34.37	34.40	34.37	34.35	34.37	34.43	34.39	34.35	34.42	34.33	34.41	34.43	34.35	34.41	34.36	34.43	34.39	34.47	34.39	34.39		
33.11	33.12	33.19	33.11	33.07	33.10	33.08	33.06	33.11	33.17	33.14	33.13	33.19	33.07	33.22	33.12	33.17	33.15	33.18	33.11	33.24		
31.96	31.91	32.01	31.89	31.79	31.89	31.86	31.85	31.83	31.80	31.94	31.76	31.75	31.85	31.92	31.81	31.93	31.89	31.91	31.87	31.90		
30.74	30.80	30.78	30.76	30.69	30.76	30.77	30.82	30.75	30.81	30.74	30.78	30.82	30.72	30.75	30.81	30.72	30.65	30.86	30.75	30.74		
29.74	29.69	29.76	29.65	29.71	29.75	29.63	29.65	29.71	29.72	29.72	29.67	29.75	29.79	29.67	29.72	29.69	29.72	29.75	29.64			
28.90	28.80	28.70	28.98	28.76	28.71	28.89	28.81	28.74	28.72	28.82	28.75	28.76	28.62	28.78	28.72	28.85	28.58	28.68				
27.73	27.74	27.75	27.74	27.75	27.78	27.79	27.74	27.74	27.63	27.85	27.69	27.77	27.71	27.73	27.74	27.76						
26.88	26.83	26.88	26.85	26.89	26.79	26.73	26.56	26.84	26.94	26.85	26.96	26.81	26.90	26.89								
26.14	26.10	26.16	26.24	26.07	26.20	26.02	26.52	26.44	26.47	26.05	26.41	26.55	26.02	26.76	26.03	26.05	26.09	26.13	26.07	26.07		
25.32	25.35	25.43	25.35	25.37	25.41	25.62	25.49	25.41	25.48	25.47	25.44	25.53	25.60	25.67	25.39	25.36	25.35	25.41	25.28			
24.58	24.59	24.64	24.53	24.64	24.73	25.53	25.50	25.41	25.33	25.37	25.38	25.44	25.44	25.65	25.80	24.64	24.65	24.67	24.63	24.73		
23.94	23.93	23.98	23.91	23.92	24.05	24.46	24.35	24.30	24.38	24.20	24.43	24.45	24.37	24.50	23.85	23.93	23.84	23.94				
23.31	23.31	23.32	23.35	24.00	24.00	24.44	24.33	24.32	24.33	24.37	24.32	24.33	24.39	24.44	24.52	24.78	23.26	23.25	23.37	23.27		
22.69	22.69	22.69	22.69	24.09	24.50	24.44	24.22	24.29	24.33	24.30	24.26	24.35	24.36	24.47	24.43	24.74	22.71	22.71	22.66	22.72		
22.14	22.07	22.09	22.10	24.70	24.91	24.54	24.39	24.29	24.34	24.33	24.26	24.33	24.38	24.46	24.55	24.75	22.15	22.04	22.16	22.09		
21.51	21.49	21.60	21.55	24.78	24.48	24.31	24.26	24.31	24.37	24.31	24.28	24.28	24.34	24.49	24.44	24.73	21.59	21.49	21.62	21.62		
20.98	21.02	21.06	21.02	24.72	24.55	24.33	24.27	24.28	24.31	24.23	24.17	24.22	24.30	24.42	24.51	24.61	21.03	21.08	21.00	20.98		
20.61	20.57	20.55	24.77	24.64	24.50	24.44	24.25	24.21	24.27	24.25	24.22	24.29	24.31	24.34	24.51	24.65	20.54	20.51	20.57	20.51		
20.07	19.98	20.03	24.63	24.55	24.43	24.35	24.23	24.21	24.23	24.24	24.23	24.20	24.45	24.46	24.47	24.67	20.01	20.12	20.04			
19.69	19.66	19.65	24.47	24.38	24.30	24.19	24.19	24.17	24.24	24.39	24.26	24.43	24.47	24.61	19.67	19.64	19.67					
19.22	19.27	19.18	19.18	19.22	19.27	19.29	19.32	19.16	19.17	19.13	19.19	19.22	19.13	19.17	19.11	19.25	19.19	19.29	19.10	19.25		
18.56	18.71	18.72	18.77	18.69	18.67	18.79	18.75	18.72	18.67	18.71	18.74	18.73	18.84	18.71	18.77	18.80	18.76	18.81	18.70	18.69		
18.36	18.28	18.39	18.42	18.34	18.28	18.36	18.34	18.47	18.36	18.37	18.41	18.41	18.31	18.31	18.36	18.39	18.35	18.29	18.39	18.48		
17.99	17.98	18.06	18.02	17.98	18.08	17.93	17.94	17.96	18.01	18.07	17.97	17.97	17.98	17.92	17.98	17.97	17.99	17.90	17.96	17.99		
17.74	17.62	17.62	17.58	17.70	17.58	17.60	17.62	17.64	17.63	17.71	17.66	17.54	17.65	17.57	17.76	17.65	17.60	17.62	17.63	17.62		

FIGURE 11

The Range Image for a Boulder at 20 m

EDGE ENHANCEMENT BASED ON FOUR DIRECTIONAL RATIO (N=2)

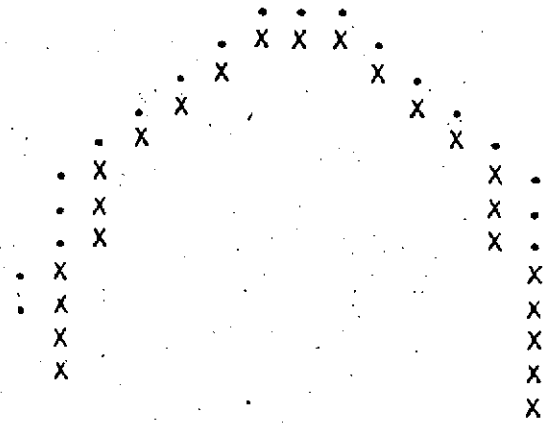

EDGE ENHANCEMENT BASED ON NORMALIZED HAMILTONIAN

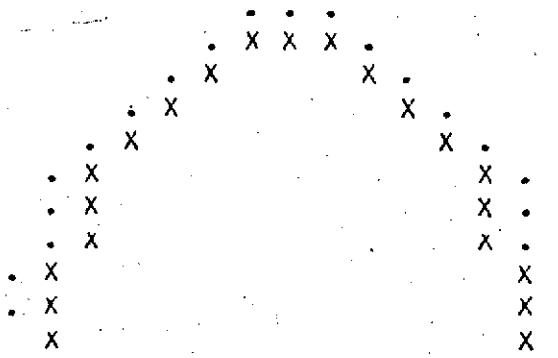

FIGURE 12

Outlines of the Boulder at 20 m

CALCULATED RANGE DATA FOR A HEMISPHERICAL BOULDER (1.00 METER RADIUS) AT A DISTANCE OF 40.00 METERS FROM MARS ROVER

BETA MAX = 4.8 DEGREES BETA MIN = 2.4 DEGREES BETA INCREMENT = .10 DEGREES
THETA MAX = 2.0 DEGREES THETA MIN = -2.0 DEGREES THETA INCREMENT = .20 DEGREES

R(1,1)-----(BETA MIN, THETA MIN)
R(25,1)-----(BETA MAX, THETA MIN)

R(1,21)-----(BETA MIN, THETA MAX)
R(25,21)-----(BETA MAX, THETA MAX)

UNDISTORTED BY NOISE

60.00	60.00	60.00	60.00	60.00	60.00	60.00	60.00	60.00	60.00	60.00	60.00	60.00	60.00	60.00	60.00	60.00	60.00	60.00	60.00	60.00
60.00	60.00	60.00	60.00	60.00	60.00	60.00	60.00	60.00	60.00	60.00	60.00	60.00	60.00	60.00	60.00	60.00	60.00	60.00	60.00	60.00
60.00	60.00	60.00	60.00	60.00	60.00	60.00	60.00	60.00	60.00	60.00	60.00	60.00	60.00	60.00	60.00	60.00	60.00	60.00	60.00	60.00
60.00	60.00	60.00	60.00	60.00	60.00	60.00	60.00	60.00	60.00	60.00	60.00	60.00	60.00	60.00	60.00	60.00	60.00	60.00	60.00	60.00
60.00	60.00	60.00	60.00	60.00	60.00	60.00	60.00	60.00	60.00	60.00	60.00	60.00	60.00	60.00	60.00	60.00	60.00	60.00	60.00	60.00
59.25	59.25	59.25	59.25	59.25	59.25	59.25	59.25	59.25	59.25	59.25	59.25	59.25	59.25	59.25	59.25	59.25	59.25	59.25	59.25	59.25
57.25	57.25	57.25	57.25	57.25	57.25	57.25	57.25	57.25	57.25	57.25	57.25	57.25	57.25	57.25	57.25	57.25	57.25	57.25	57.25	57.25
55.50	55.50	55.50	55.50	55.50	55.50	55.50	55.50	55.50	55.50	55.50	55.50	55.50	55.50	55.50	55.50	55.50	55.50	55.50	55.50	55.50
53.75	53.75	53.75	53.75	53.75	53.75	53.75	53.75	53.75	53.75	53.75	53.75	53.75	53.75	53.75	53.75	53.75	53.75	53.75	53.75	53.75
52.13	52.13	52.13	52.13	52.13	52.13	52.13	52.13	52.13	52.13	52.13	52.13	52.13	52.13	52.13	52.13	52.13	52.13	52.13	52.13	52.13
50.50	50.50	50.50	50.50	50.50	50.50	50.50	50.50	50.50	50.50	50.50	50.50	50.50	50.50	50.50	50.50	50.50	50.50	50.50	50.50	50.50
49.13	49.13	49.13	49.13	49.13	49.13	49.13	49.13	49.13	49.13	49.13	49.13	49.13	49.13	49.13	49.13	49.13	49.13	49.13	49.13	49.13
47.75	47.75	47.75	47.75	47.75	47.75	47.75	47.75	47.75	47.75	47.75	47.75	47.75	47.75	47.75	47.75	47.75	47.75	47.75	47.75	47.75
46.50	46.50	46.50	46.50	46.50	46.50	46.50	46.50	46.50	46.50	46.50	46.50	46.50	46.50	46.50	46.50	46.50	46.50	46.50	46.50	46.50
45.25	45.25	45.25	45.25	45.25	45.25	45.25	45.25	45.25	45.25	45.25	45.25	45.25	45.25	45.25	45.25	45.25	45.25	45.25	45.25	45.25
44.13	44.13	44.13	44.13	44.13	44.13	44.13	44.13	44.13	44.13	44.13	44.13	44.13	44.13	44.13	44.13	44.13	44.13	44.13	44.13	44.13
43.06	43.06	43.06	43.06	43.06	43.06	43.06	43.06	43.06	43.06	43.06	43.06	43.06	43.06	43.06	43.06	43.06	43.06	43.06	43.06	43.06
41.94	41.94	41.94	41.94	41.94	41.94	41.94	41.94	41.94	41.94	41.94	41.94	41.94	41.94	41.94	41.94	41.94	41.94	41.94	41.94	41.94
40.94	40.94	40.94	40.94	40.94	40.94	40.94	40.94	40.94	40.94	40.94	40.94	40.94	40.94	40.94	40.94	40.94	40.94	40.94	40.94	40.94
40.06	40.06	40.06	40.06	40.06	40.06	40.06	40.06	40.06	40.06	40.06	40.06	40.06	40.06	40.06	40.06	40.06	40.06	40.06	40.06	40.06
39.13	39.13	39.13	39.13	39.13	39.13	39.13	39.13	39.13	39.13	39.13	39.13	39.13	39.13	39.13	39.13	39.13	39.13	39.13	39.13	39.13
38.25	38.25	38.25	38.25	38.25	38.25	38.25	38.25	38.25	38.25	38.25	38.25	38.25	38.25	38.25	38.25	38.25	38.25	38.25	38.25	38.25
37.38	37.38	37.38	37.38	37.38	37.38	37.38	37.38	37.38	37.38	37.38	37.38	37.38	37.38	37.38	37.38	37.38	37.38	37.38	37.38	37.38
36.63	36.63	36.63	36.63	36.63	36.63	36.63	36.63	36.63	36.63	36.63	36.63	36.63	36.63	36.63	36.63	36.63	36.63	36.63	36.63	36.63
35.88	35.88	35.88	35.88	35.88	35.88	35.88	35.88	35.88	35.88	35.88	35.88	35.88	35.88	35.88	35.88	35.88	35.88	35.88	35.88	35.88

CONTAMINATED BY ZERO MEAN, .05 METER STANDARD DEVIATION, GAUSSIAN NOISE

59.97	60.03	60.02	60.01	59.98	59.97	60.05	60.01	59.97	60.05	59.95	60.04	60.10	59.97	60.03	59.99	60.11	60.02	60.10	60.02	60.01
59.98	60.00	60.07	59.98	59.94	59.97	59.96	59.93	59.98	60.05	60.01	60.01	60.06	59.94	60.10	60.00	60.04	60.02	60.06	59.98	60.11
60.08	60.06	60.13	60.01	59.92	60.02	60.01	59.97	59.96	59.93	60.07	59.91	60.07	59.97	60.05	59.93	60.03	60.11	60.03	59.94	60.03
59.99	60.05	60.03	59.98	59.90	60.01	60.02	60.07	60.00	60.05	59.99	60.03	60.07	59.97	60.00	60.06	59.97	59.90	60.11	60.00	59.99
60.05	60.01	60.02	59.97	60.02	60.07	59.94	59.89	60.03	59.98	59.97	59.88	59.92	60.06	60.11	59.96	60.03	60.00	60.03	60.06	59.95
59.26	59.23	59.26	59.24	59.32	59.27	59.25	59.17	59.21	59.25	59.25	59.17	59.25	59.31	59.32	59.18	59.34	59.28	59.21	59.15	59.24
57.23	57.24	57.23	57.24	57.25	57.26	57.25	57.22	57.24	57.25	57.25	57.25	57.25	57.23	57.22	57.19	57.29	57.21	57.23	57.24	57.26
55.51	55.45	55.50	55.47	55.51	55.41	55.41	55.49	55.50	55.47	55.50	55.49	55.53	55.49	55.53	55.47	55.47	55.47	55.58	55.44	55.51
53.77	53.72	53.79	53.80	53.69	53.79	53.67	53.52	53.42	53.49	53.52	53.39	53.49	53.52	53.49	53.40	53.81	53.71	53.67	53.71	53.75
52.07	52.11	52.18	52.10	52.16	52.06	52.12	52.47	52.38	52.36	52.43	52.40	52.50	52.57	52.67	52.70	52.14	52.11	52.10	52.16	52.03
50.46	50.43	50.52	50.48	50.51	50.75	50.51	50.46	50.36	50.27	50.31	50.32	50.39	50.40	50.43	50.81	50.52	50.52	50.55	50.50	50.60
49.13	49.17	49.17	49.10	49.12	49.03	49.42	49.50	49.50	49.31	49.32	49.19	49.43	49.40	49.53	49.63	49.12	49.04	49.12	49.02	49.13
47.74	47.74	47.76	47.74	47.82	47.56	47.37	47.27	47.26	47.23	47.22	47.25	47.24	47.33	47.38	47.48	47.80	47.70	47.69	47.80	47.71
46.46	46.50	46.47	46.50	46.68	46.45	46.37	46.14	46.22	46.23	46.21	46.26	46.27	46.41	46.36	46.72	46.52	46.53	46.48	46.46	46.54
45.27	45.19	45.22	45.23	45.60	45.44	45.40	45.30	45.21	45.25	45.24	45.17	45.21	45.33	45.37	45.48	45.70	45.26	45.16	45.29	45.22
44.07	44.05	44.17	44.11	44.72	44.40	44.23	44.17	44.23	44.26	44.21	44.19	44.11	44.25	44.41	44.36	44.64	44.15	44.05	44.18	44.18
42.98	43.02	43.08	43.08	43.87	43.65	43.24	43.18	43.18	43.20	43.10	43.08	43.13	43.21	43.33	43.42	43.53	43.31	43.08	43.00	42.98
41.90	41.95	41.91	41.91	42.76	43.55	43.41	43.35	43.14	43.16	43.17	43.15	43.13	43.19	43.20	43.24	43.42	43.56	43.90	41.89	41.95	41.88
40.84	40.85	40.94	41.04	42.69	43.48	43.30	43.25	43.13	43.11	43.17	43.15	43.15	43.12	43.18	43.34	43.38	43.56	43.77	40.88	41.00	40.91
40.13	40.12	40.09	40.02	42.62	43.50	43.35	43.27	43.17	43.23	43.06	43.05	43.11	43.27	43.15	43.31	43.36	43.52	43.77	40.11	40.07	40.11
39.16	39.21	39.11	39.12	39.13	39.21	39.25	39.12	43.04	43.00	43.03	43.07	43.10	39.12	43.24	43.17	39.12	39.23	39.04	39.19	
36.16	36.21	36.22	36.27	36.19	36.17	36.29	36.25	36.22	36.17	36.21	36.24	36.25	36.34	36.21	36.27	36.30	36.26	36.31	36.20	36.19
37.36	37.36	37.39	37.42	37.24	37.28	37.36	37.34	37.47	37.36	37.37	37.41	37.41	37.31	37.31	37.36	37.39	37.35	37.28	37.39	37.46
36.64	36.69	36.72	36.68	36.63	36.74	36.59	36.60	36.62	36.67	36.73	36.62	36.62	36.64	36.58	36.64	36.63	36.65	36.56	36.62	36.64
35.99	35.87	35.87	35.83	35.95	35.81	35.89	35.87	35.89	35.88	35.96	35.91	35.79	35.90	35.82	36.03	35.90	35.85	35.87	35.88	35.87

FIGURE 13

The Range Image for a Boulder at 40 m

EDGE ENHANCEMENT BASED ON FOUR DIRECTIONAL RATIO (N=2)

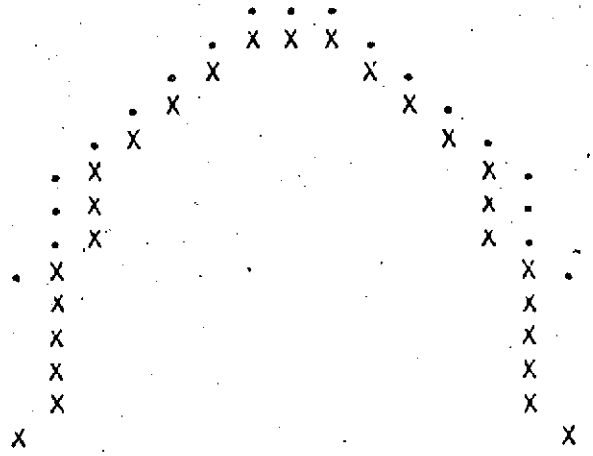

EDGE ENHANCEMENT BASED ON NORMALIZED HAMILTONIAN

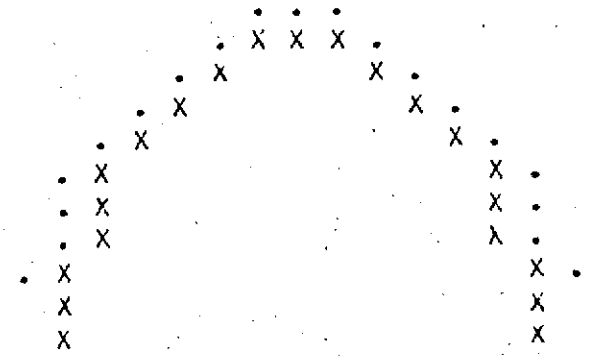

FIGURE 14

Outlines of the Boulder at 40 m

maxima compared to the ranges slightly above and slightly below them in the range image. For the case of the 1 meter radius, hemispherical boulder, located 30 meters from the Rover, Figures 15 and 16 detail the "before" and "after" outlines of the boulder. Note that the scaling of the computer printout has been changed from that of Figure 8, to show the outcomes more clearly. Although only a few bottom edge points (seen as "-") are available in Figure 16, these are really all that are necessary to provide an indication of the complete bottom edge for the purpose of size determination. This scheme would seem to perform satisfactorily; however, it was the noiseless range values which were being compared in order to find the bottom edge in this case. When the more realistic noisy range values are used in the comparison, the result is as in Figure 17; the picture in this case is obviously unacceptable. The explanation for the degradation in performance is that the range values measured to the bottom edge are no more than .01 meters larger than their adjacent elements in the range image, so that the standard deviation of noise of .05 meters completely obscures this difference.

In seeking a more noise-resistant scheme, the following procedure was developed. By examining each range value lying along the center of the measurement matrix (which corresponds to an aximuth angle of zero, directly in the Rover's direction of travel) and comparing them to the range readings that would be takne if the boulder were not present, the bottom edge point for the center column of the range image can be detected if a given element <u>is not</u> "close" to the range without the boulder (given by equation (12), $r_{i,j} = 3/\sin\beta$) and the element just below this one <u>is</u> "close" to the range without the

EDGE ENHANCEMENT BASED ON FOUR DIRECTIONAL RATIO (N=2)

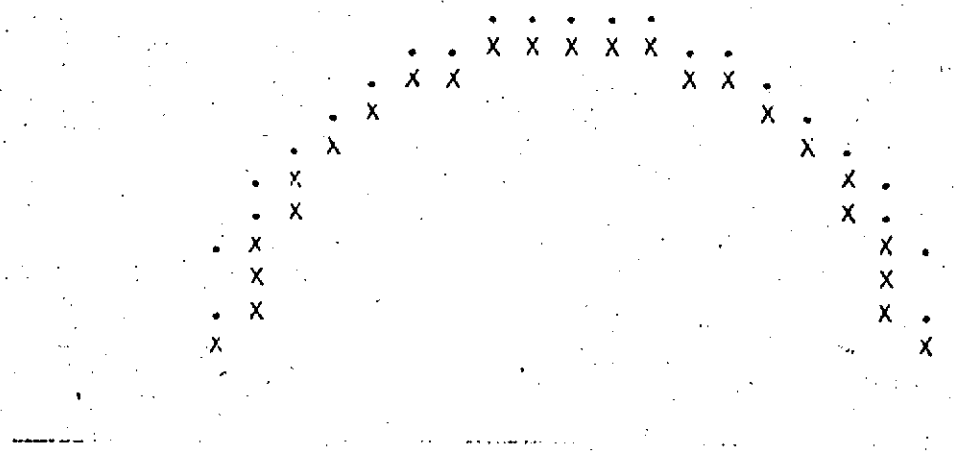

EDGE ENHANCEMENT BASED ON NORMALIZED HAMILTONIAN

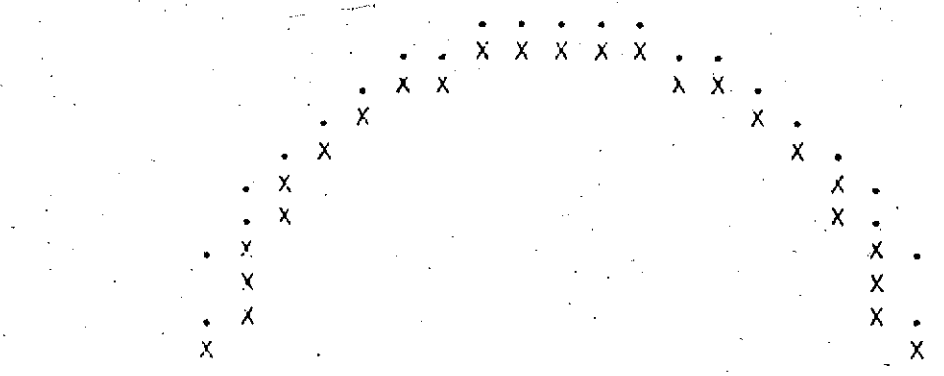

FIGURE 15

Expanded Scale - The Boulder at 30 m

EDGE ENHANCEMENT BASED ON FOUR DIRECTIONAL RATIO (N=2)

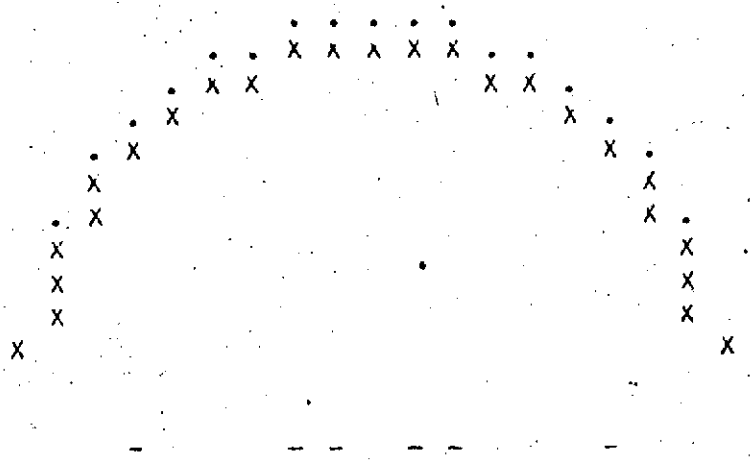

EDGE ENHANCEMENT BASED ON NORMALIZED HAMILTONIAN

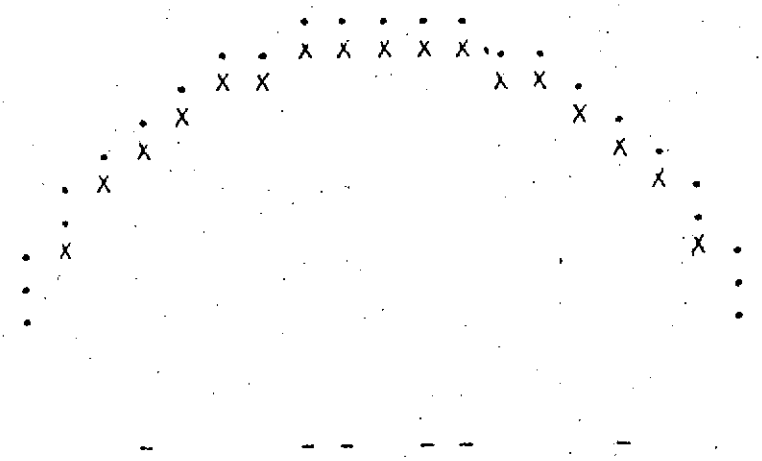

FIGURE 16

The Bottom Edge of the Boulder at 30 m - No Noise

EDGE ENHANCEMENT BASED ON FOUR DIRECTIONAL RATIO (N=2)

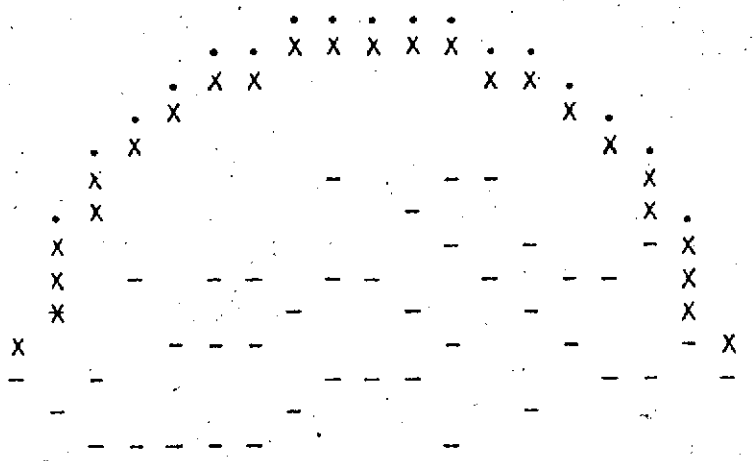

EDGE ENHANCEMENT BASED ON NORMALIZED HAMILTONIAN

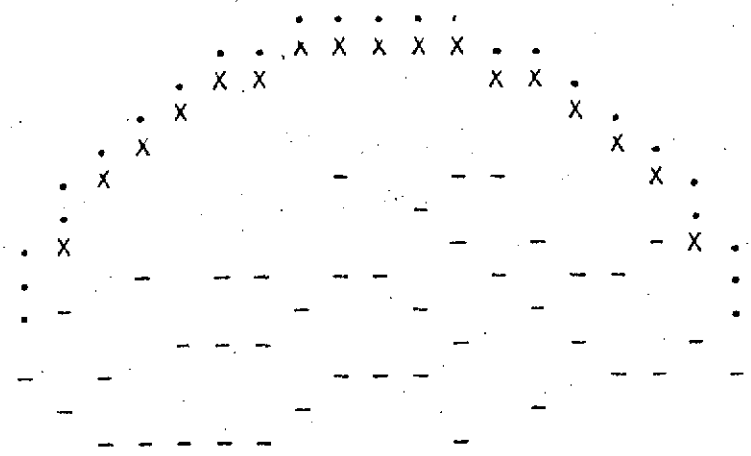

FIGURE 17

The Bottom Edge of the Boulder at 30 m - With Noise

boulder. By "close" we are considering the effects of noise, so that the range without the boulder will be taken as anything between the limits of $(3/\sin\beta) \pm 3\sigma_v$. Once this bottom edge point is found, we may use a linear interpolation to fill in the edge between this point and the two points on either side of the boulder determined by the original edge detection scheme to be closest to the bottom.

Returning to our example of the boulder at 30 meters, the range values used for this bottom edge scheme are listed in Table 1. Notice that for i = 20 the true range measurement, under the heading RWB (BETA, THETA), does not fall within the limits of $(3/\sin\beta) \pm 3\sigma_v$, under the headings of RWOB (BETA)-.15 and RWOB (BETA) + .15, but that for i = 21 the range measurement does fall within these limits. Therefore, the bottom edge point is located in the center of the range image at i = 21. The lowest points on the boulder that can be seen by means of the edge detection algorithms are indexed (17,5) and (17,17). So by joining these three points with two vertical lines (for the sides of the boulder) and one horizontal line (for the bottom of the boulder), we obtain the picture of Figure 18. While the results for this scenario are excellent, a serious practical problem can be envisioned. If the terrain in front of the boulder is not as flat and smooth as assumed, for example if there are some small pebbles on the terrain directly in front of the boulder, then it is obvious that the bottom edge scheme just outlined will very likely give a false indication. This procedure must therefore be considered unfeasible.

The conclusion to be drawn from these investigations is that the bottom edge problem will have to be approached by a completely

TABLE 1

Range Values Used in Bottom Edge Determination

RANGE VALUES USED FOR BOTTOM EDGE ALGORITHM

BETA MIN = 3.0 DEGREES
BETA INCREMENT = .15 DEGREES
BETA = BETA MIN + (I-1)*BETA INCREMENT
THETA = 0.0 DEGREES (DIRECTLY IN FRONT OF MARS ROVER)

RWOB(BETA) = TRUE RANGE FROM LASER TO THE GROUND, WITHOUT THE BOULDER PRESENT, AS A FUNCTION OF BETA ONLY (=3.0/SIN(BETA))
RWOB(BETA)+.15 = TRUE RANGE WITHOUT THE BOULDER, PLUS 3*(STANDARD DEVIATION OF NOISE)
RWOB(BETA)-.15 = TRUE RANGE WITHOUT THE BOULDER, MINUS 3*(STANDARD DEVIATION OF NOISE)
RWB(BETA,THETA) = RANGE FROM LASER, WITH THE BOULDER PRESENT, AS A FUNCTION OF BETA AND THETA

I	BETA	RWOB(BETA)	RWOB(BETA)+.15	RWOB(BETA)-.15	RWB(BETA,THETA)
1	3.00	57.25	57.40	57.10	57.20
2	3.15	54.63	54.77	54.47	54.64
3	3.30	52.13	52.27	51.97	52.19
4	3.45	49.88	50.02	49.72	49.87
5	3.60	47.75	47.90	47.60	47.74
6	3.75	45.88	46.02	45.72	45.85
7	3.90	44.13	44.27	43.97	29.75
8	4.05	42.50	42.65	42.35	29.69
9	4.20	40.94	41.09	40.79	29.59
10	4.35	39.50	39.65	39.35	29.49
11	4.50	38.25	38.40	38.10	29.36
12	4.65	37.06	37.21	36.91	29.36
13	4.80	35.88	36.02	35.72	29.35
14	4.95	34.75	34.90	34.60	29.26
15	5.10	33.75	33.90	33.60	29.27
16	5.25	32.75	32.90	32.60	29.24
17	5.40	31.88	32.02	31.72	29.13
18	5.55	31.06	31.21	30.91	29.18
19	5.70	30.25	30.40	30.10	29.17
20	5.85	29.44	29.59	29.29	29.09
21	6.00	28.69	28.84	28.54	28.63
22	6.15	28.03	28.18	27.88	28.00
23	6.30	27.38	27.52	27.22	27.37
24	6.45	26.69	26.84	26.54	26.79
25	6.60	26.13	26.27	25.97	26.21

EDGE ENHANCEMENT BASED ON FOUR DIRECTIONAL RATIO (N=2)

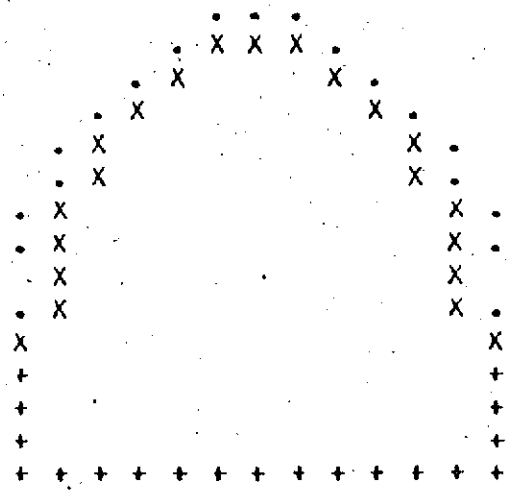

EDGE ENHANCEMENT BASED ON NORMALIZED HAMILTONIAN

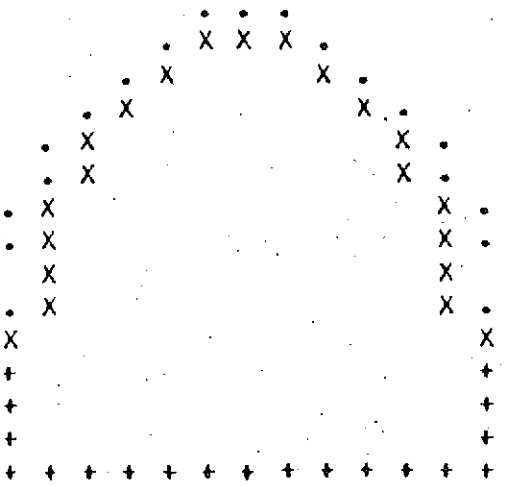

FIGURE 18

The Interpolated Bottom Edge for a Boulder at 30 m

different method. The use of gradient comparisons seems like the next logical step, and this is the direction that will be taken in future research efforts.

6. SCANNING SCHEME CONSIDERATIONS

To this point the scanning angle limits have been chosen with the a priori knowledge of the boulder's size and location, so that, for a fixed number of elevation and aximuth angles to be scanned (i.e., for a fixed number of elements in the range image), the angle differences between the range points were as small as possible, in order to maximize the information received about the boulder and its immediate surroundings. The geometry defining the angle limits for this variable scanning procedure is illustrated in Figure 19. Based on this drawing, the following equations can be derived,

$$\beta_{min} = \sin^{-1}\left[\frac{3\sqrt{b^2 + 9 - r^2} - br}{b^2 + 9}\right] \tag{53}$$

$$\beta_{max} = \tan^{-1}\left[\frac{3}{b-r}\right] \tag{54}$$

$$\theta_{max} = \sin^{-1}\left[\frac{r}{b}\right] \tag{55}$$

$$\theta_{min} = -\theta_{max} \tag{56}$$

As expected, these equations exhibit functional dependence on b and r.

A compilation of these angle limits for a number of different size and location boulders was then generated, and the results are listed in Table 2. The column headed "Extreme Theta" refers to the magnitude of either θ_{max} or θ_{min} since they are the same; the sign of these limits is as defined in equations (55) and (56). The additional columns headed "Max Range" and "Min Range" give a measure of the limits on the range measurements necessary to detect these various mid-range

TABLE 2

Range and Angle Limits Calculated for Variable Scanning

DISTANCE	RADIUS	MAX RANGE	MIN RANGE	MIN BETA	MAX BETA	EXTREME THETA
10.0	0.25	11.35	10.20	15.33	17.10	1.43
10.0	0.50	12.44	9.96	13.95	17.53	2.87
10.0	0.75	13.77	9.72	12.53	17.97	4.30
10.0	1.00	15.44	9.49	11.20	18.43	5.74
10.0	1.25	17.58	9.25	9.82	18.92	7.18
10.0	1.50	20.44	9.01	8.44	19.44	8.63
10.0	1.75	24.44	8.78	7.05	19.98	10.08
10.0	2.00	30.44	8.54	5.66	20.56	11.54
20.0	0.25	22.04	19.98	7.82	8.64	0.72
20.0	0.50	24.22	19.73	7.11	8.75	1.43
20.0	0.75	26.89	19.48	6.41	8.86	2.15
20.0	1.00	30.22	19.24	5.70	8.97	2.87
20.0	1.25	34.51	18.99	4.99	9.09	3.58
20.0	1.50	40.22	18.74	4.28	9.21	4.30
20.0	1.75	48.22	18.49	3.57	9.33	5.02
20.0	2.00	60.22	18.25	2.86	9.46	5.74
30.0	0.25	32.98	29.90	5.24	5.76	0.48
30.0	0.50	36.15	29.65	4.76	5.81	0.95
30.0	0.75	40.15	29.40	4.29	5.86	1.43
30.0	1.00	45.15	29.15	3.81	5.91	1.91
30.0	1.25	51.58	28.91	3.33	5.96	2.39
30.0	1.50	60.15	28.66	2.86	6.01	2.87
30.0	1.75	72.15	28.41	2.38	6.06	3.34
30.0	2.00	90.15	28.16	1.91	6.12	3.82
40.0	0.25	43.75	39.86	3.93	4.32	0.36
40.0	0.50	48.11	39.61	3.57	4.34	0.72
40.0	0.75	53.45	39.36	3.22	4.37	1.07
40.0	1.00	60.11	39.12	2.86	4.40	1.43
40.0	1.25	68.68	38.87	2.50	4.43	1.79
40.0	1.50	80.11	38.62	2.15	4.46	2.15
40.0	1.75	96.11	38.37	1.79	4.48	2.51
40.0	2.00	*****	38.12	1.43	4.51	2.87

obstacles. The appropriate formulae are, from equation (12),

$$\text{Max Range} = \frac{3}{\sin \beta_{min}} \tag{57}$$

$$\text{Min Range} = \frac{3}{\sin \beta_{max}} \tag{58}$$

In practice these angle limits should be expanded somewhat, so that a number of range measurements to the terrain surrounding the boulder can also be made (after all, the edge detection algorithms must compare range values on the terrain to those on the boulder in order to enhance the edge). The actual limits used in the simulation program for the four different test cases (as pictured in Figures 8, 10, 12, and 14) are given in Table 3.

In reality, the information about the size and location of boulders to be detected will obviously not be available. However, it may be possible to specify the limits on the location of obstacles in the mid-range field that we expect the laser rangefinder to be able to detect, and pick the limits on the angles to scan this entire field. While this type of scanning scheme will be suboptimal with respect to the edge detection algorithms, it nonetheless respresents a first attempt at a physically realizable procedure.

To simulate the situation where the angle limits are fixed so as to include any 1 meter radius boulder between 10 and 40 meters from the vehicle, the geometry of Figure 20 was defined. From this picture it is obvious that all smaller boulders, and some larger boulders, between these limits will also be scanned, so that this type of scanning scheme is rather versatile. The scanning angle limits can now be de-

TABLE 3

Angle Limits Implemented for Variable Scanning

DISTANCE	RADIUS	MAX BETA	MIN BETA	EXTREME THETA
10	1.0	19.6°	10.0°	7.0°
20	1.0	9.8°	5.0°	4.0°
30	1.0	6.6°	3.0°	3.0°
40	1.0	4.8°	2.4°	2.0°

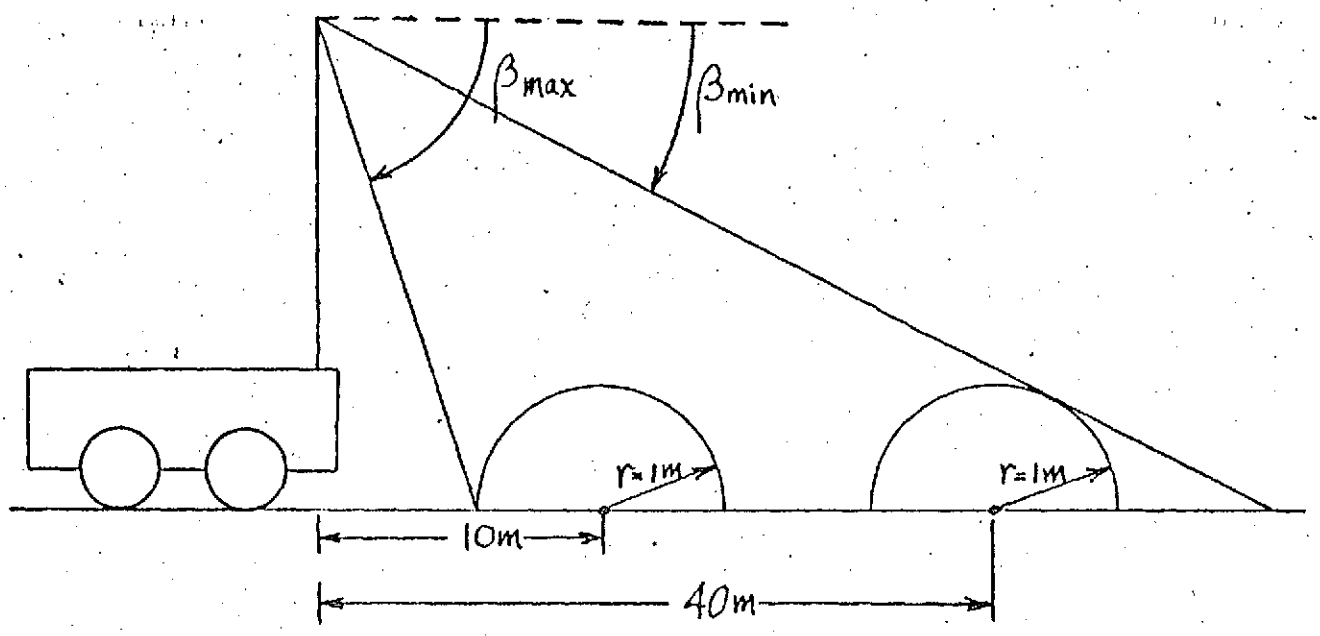

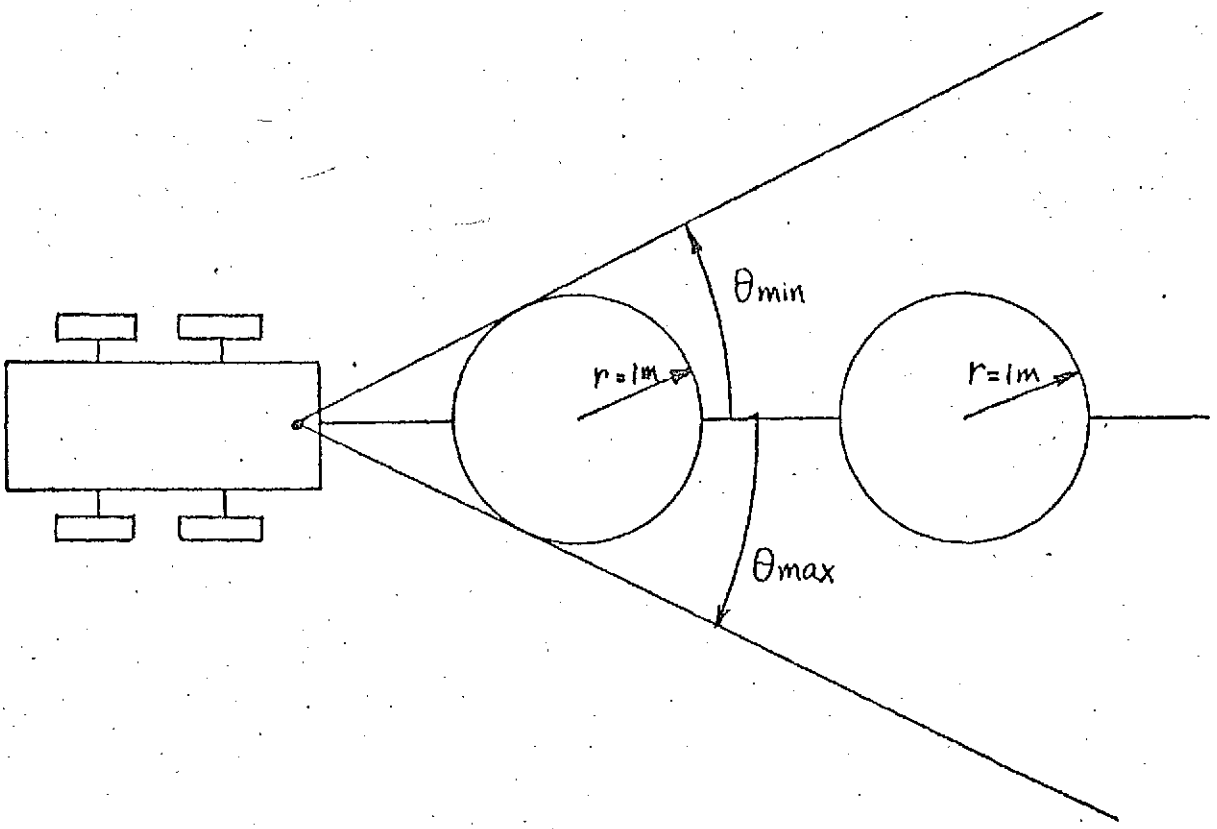

FIGURE 20

Geometry for Fixed Scanning

termined from equations (53) through (56) by substituting in the appropriate values of b and r, i.e.

$$\beta_{min}\ (b = 40,\ r = 1) = 2.86^{\circ} \tag{59}$$

$$\beta_{max}\ (b = 10,\ r = 1) = 18.43^{\circ} \tag{60}$$

$$\theta_{max}\ (b = 10,\ r = 1) = 5.74^{\circ} \tag{61}$$

$$\theta_{min}\ (b = 10,\ r = 1) = -\theta_{max}(b = 10,\ r = 1) \tag{62}$$

The four test boulders (located at 10 m, 20 m, 30 m, and 40 m) were then scanned by this method in simulations, and the edge detection algorithms applied, to arrive at the outlines shown in Figures 21 through 24 (which should be compared to the outcomes of the variable scanning scheme illustrated in Figures 10, 12, 8, and 14 respectively). For boulders beyond the 20 m range the fixed scan technique is quite unacceptable for the edge detection scheme, as the resulting boulder outlines are too incomplete to provide useful information for path selection (except possibly as a go-no go indication of whether or not there is some type of obstacle in the vehicle's path of travel at the longer ranges). Once again, this problem will require further investigation.

EDGE ENHANCEMENT BASED ON FOUR DIRECTIONAL RATIO (N=2)

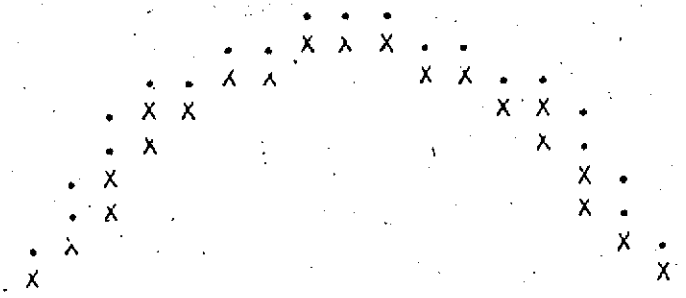

EDGE ENHANCEMENT BASED ON NORMALIZED HAMILTONIAN

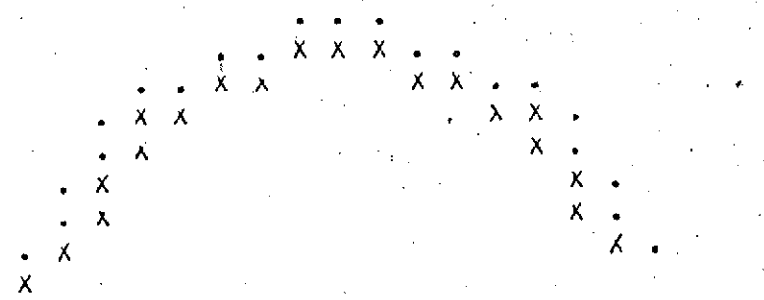

FIGURE 21

The Boulder at 10 m - Fixed Scanning

EDGE ENHANCEMENT BASED ON FOUR DIRECTIONAL RATIO (N=2)

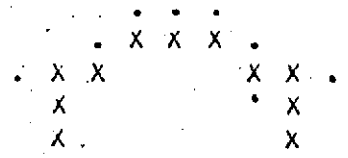

EDGE ENHANCEMENT BASED ON NORMALIZED HAMILTONIAN

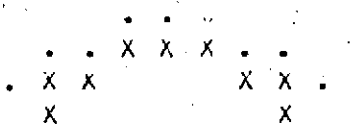

FIGURE 22

The Boulder at 20 m - Fixed Scanning

EDGE ENHANCEMENT BASED ON FOUR DIRECTIONAL RATIO (N=2)

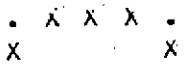

EDGE ENHANCEMENT BASED ON NORMALIZED HAMILTONIAN

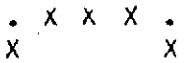

FIGURE 23

The Boulder at 30 m - Fixed Scanning

FOUR ENHANCEMENT BASED ON FOUR DIRECTIONAL RATIO (N=2)

X X

ECCE ENHANCEMENT BASED ON NORMALIZED HAMILTONIAN

FIGURE 24

The Boulder at 40 m - Fixed Scanning

7. SIMULATION RESULTS FOR CRATERS

Since the Rover will evidently encounter negative type obstacles (those extending below the terrain surface) as well as the positive type obstacles previously discussed, the edge detection scheme was tested on a representative obstacle from this second major class. A hemispherical crater of 1 meter radius, located 30 meters from the Rover directly in its path of travel, was placed on the terrain, and the geometry necessary to obtain the range values was developed in a manner similar to that for the boulder. As before, the steps in the edge detection scheme were then carried out. Figure 25 illustrates the resulting range images, both noiseless and noisy. In Figures 26 and 27 are the four alpha matrices necessary for selection of threshold values. Figure 28 shows the results of applying both the Four Directional Ratio algorithm (with $n = 2$) and the Normalized Laplacian algorithm to the noisy range image. Finally, in Figure 29, we see the outlines of the crater after the thresholding operation has been carried out for the previous matrices.

The striking feature of these pictures is that only the near edge of the crater is detected; the far edge is missed, just as the bottom edge of the boulder was missed, and for the same reason. Therefore, if the bottom edge problem of the boulder can be solved, then the far edge problem of the crater will also be solved, so that the edge detection scheme will indeed be useful for both types of obstacles.

CALCULATED RANGE DATA FOR A HEMISPHERICAL CRATER (1.00 METER RADIUS) AT A DISTANCE OF 30.00 METERS FROM MARS ROVER

BETA MAX = 6.4 DEGREES BETA MIN = 5.2 DEGREES BETA INCREMENT = .05 DEGREES
THETA MAX = 3.0 DEGREES THETA MIN = -3.0 DEGREES THETA INCREMENT = .30 DEGREES

R(1,1)-----(BETA MIN, THETA MIN)
R(25,1)-----(BETA MAX, THETA MIN)

R(1,21)-----(BETA MIN, THETA MAX)
R(25,21)-----(BETA MAX, THETA MAX)

UNDISTORTED BY NOISE

33.13	33.13	33.13	33.13	33.13	33.13	33.13	33.13	33.13	33.13	33.13	33.13	33.13	33.13	33.13	33.13	33.13	33.13	33.13	33.13	33.13
32.75	32.75	32.75	32.75	32.75	32.75	32.75	32.75	32.75	32.75	32.75	32.75	32.75	32.75	32.75	32.75	32.75	32.75	32.75	32.75	32.75
32.50	32.50	32.50	32.50	32.50	32.50	32.50	32.50	32.50	32.50	32.50	32.50	32.50	32.50	32.50	32.50	32.50	32.50	32.50	32.50	32.50
32.13	32.13	32.13	32.13	32.13	32.13	32.13	32.13	32.13	32.13	32.13	32.13	32.13	32.13	32.13	32.13	32.13	32.13	32.13	32.13	32.13
31.88	31.88	31.88	31.88	31.88	31.88	31.88	31.88	31.88	31.88	31.88	31.88	31.88	31.88	31.88	31.88	31.88	31.88	31.88	31.88	31.88
31.63	31.63	31.63	31.63	31.63	31.63	31.63	31.63	31.63	31.63	31.63	31.63	31.63	31.63	31.63	31.63	31.63	31.63	31.63	31.63	31.63
31.25	31.25	31.25	31.25	31.25	31.25	31.25	31.25	31.25	31.25	31.25	31.25	31.25	31.25	31.25	31.25	31.25	31.25	31.25	31.25	31.25
31.06	31.06	31.06	31.06	31.06	31.06	31.06	31.06	31.06	31.06	31.06	31.06	31.06	31.06	31.06	31.06	31.06	31.06	31.06	31.06	31.06
30.75	30.75	30.75	30.75	30.75	30.75	30.75	30.75	30.75	30.75	30.75	30.75	30.75	30.75	30.75	30.75	30.75	30.75	30.75	30.75	30.75
30.50	30.50	30.50	30.50	30.50	30.50	30.50	30.50	30.50	30.50	30.50	30.50	30.50	30.50	30.50	30.50	30.50	30.50	30.50	30.50	30.50
30.25	30.25	30.25	30.25	30.25	30.25	30.25	30.25	30.25	30.25	30.25	30.25	30.25	30.25	30.25	30.25	30.25	30.25	30.25	30.25	30.25
29.94	29.94	29.94	29.94	30.46	30.74	30.90	31.01	31.08	31.12	31.13	31.12	31.08	31.01	30.90	30.74	30.46	29.94	29.94	29.94	29.94
29.69	29.69	29.69	29.69	30.44	30.73	30.89	31.00	31.06	31.10	31.12	31.10	31.06	31.00	30.89	30.73	30.44	29.69	29.69	29.69	29.69
29.44	29.44	29.44	29.44	30.41	30.71	30.88	30.98	31.05	31.09	31.10	31.09	31.05	30.98	30.88	30.71	30.41	29.44	29.44	29.44	29.44
29.19	29.19	29.19	29.19	30.38	30.69	30.86	30.96	31.03	31.07	31.07	31.07	31.03	30.96	30.86	30.69	30.38	29.19	29.19	29.19	29.19
28.94	28.94	28.94	28.94	28.94	28.94	28.94	28.94	28.94	28.94	28.94	28.94	28.94	28.94	28.94	28.94	28.94	28.94	28.94	28.94	28.94
28.69	28.69	28.69	28.69	28.69	28.69	28.69	28.69	28.69	28.69	28.69	28.69	28.69	28.69	28.69	28.69	28.69	28.69	28.69	28.69	28.69
28.50	28.50	28.50	28.50	28.50	28.50	28.50	28.50	28.50	28.50	28.50	28.50	28.50	28.50	28.50	28.50	28.50	28.50	28.50	28.50	28.50
28.25	28.25	28.25	28.25	28.25	28.25	28.25	28.25	28.25	28.25	28.25	28.25	28.25	28.25	28.25	28.25	28.25	28.25	28.25	28.25	28.25
28.03	28.03	28.03	28.03	28.03	28.03	28.03	28.03	28.03	28.03	28.03	28.03	28.03	28.03	28.03	28.03	28.03	28.03	28.03	28.03	28.03
27.75	27.75	27.75	27.75	27.75	27.75	27.75	27.75	27.75	27.75	27.75	27.75	27.75	27.75	27.75	27.75	27.75	27.75	27.75	27.75	27.75
27.56	27.56	27.56	27.56	27.56	27.56	27.56	27.56	27.56	27.56	27.56	27.56	27.56	27.56	27.56	27.56	27.56	27.56	27.56	27.56	27.56
27.38	27.38	27.38	27.38	27.38	27.38	27.38	27.38	27.38	27.38	27.38	27.38	27.38	27.38	27.38	27.38	27.38	27.38	27.38	27.38	27.38
27.13	27.13	27.13	27.13	27.13	27.13	27.13	27.13	27.13	27.13	27.13	27.13	27.13	27.13	27.13	27.13	27.13	27.13	27.13	27.13	27.13
26.88	26.88	26.88	26.88	26.88	26.88	26.88	26.88	26.88	26.88	26.88	26.88	26.88	26.88	26.88	26.88	26.88	26.88	26.88	26.88	26.88

CONTAMINATED BY ZERO MEAN, .05 METER STANDARD DEVIATION, GAUSSIAN NOISE

33.10	33.12	33.15	33.14	33.13	33.12	33.10	33.17	33.17	33.17	33.08	33.16	33.23	33.13	33.16	33.11	33.23	33.14	33.22	33.14	33.14
32.73	32.75	32.82	32.73	32.69	32.72	32.71	32.68	32.73	32.83	32.78	32.76	32.81	32.84	32.85	32.75	32.79	32.77	32.81	32.73	32.66
32.56	32.54	32.63	32.51	32.42	32.52	32.51	32.47	32.46	32.43	32.57	32.41	32.57	32.47	32.55	32.43	32.53	32.51	32.53	32.49	32.53
32.12	32.17	32.15	32.14	32.02	32.13	32.14	32.20	32.12	32.17	32.12	32.16	32.19	32.09	32.13	32.18	32.09	32.03	32.24	32.13	32.11
31.92	31.83	31.89	31.84	31.90	31.95	31.81	31.77	31.93	31.80	31.87	31.75	31.79	31.93	31.98	31.86	31.91	31.88	31.91	31.94	31.82
31.74	31.80	31.84	31.82	31.84	31.83	31.83	31.84	31.84	31.84	31.80	31.86	31.82	31.88	31.78	31.90	31.72	31.85	31.59	31.52	31.62
31.23	31.24	31.25	31.24	31.25	31.28	31.29	31.27	31.27	31.23	31.16	31.25	31.25	31.23	31.22	31.19	31.29	31.21	31.23	31.24	31.26
31.07	31.01	31.07	31.03	31.07	30.97	31.07	31.03	31.03	31.03	31.10	31.10	31.03	31.07	31.08	31.03	31.04	31.14	31.00	31.09	31.08
30.77	30.72	30.79	30.68	30.69	30.81	30.81	30.84	31.00	31.12	31.21	31.05	31.11	31.03	30.95	30.75	30.87	30.71	30.75	30.69	30.70
30.44	30.44	30.55	30.47	30.47	30.63	30.63	30.65	31.03	31.07	31.19	31.14	31.15	31.08	30.94	30.77	30.52	30.49	30.47	30.53	30.41
30.21	30.18	30.27	30.23	30.27	30.25	30.23	31.03	31.07	31.03	31.12	31.11	31.10	30.97	30.96	30.81	30.45	30.27	30.30	30.25	30.35
29.94	29.98	29.98	29.91	30.45	30.72	30.84	30.92	31.05	31.14	31.17	30.78	31.15	31.03	30.95	30.73	30.46	29.95	29.93	29.84	29.94
29.68	29.68	29.70	29.72	30.41	30.71	30.85	30.93	31.04	31.07	31.20	31.11	31.12	30.99	30.84	30.63	30.31	29.94	29.83	29.74	29.85
29.40	29.44	29.41	29.44	30.38	30.69	30.82	30.93	31.03	31.11	31.13	31.09	31.04	30.90	30.80	30.57	30.34	29.46	29.46	29.41	29.47
29.20	29.13	29.16	29.22	30.36	30.65	30.87	31.00	31.05	31.14	31.15	31.06	31.03	30.90	30.80	30.59	30.37	29.21	29.10	29.23	29.15
28.88	28.87	28.96	28.93	29.02	29.07	28.89	28.97	29.09	29.03	29.17	28.88	28.95	29.12	28.96	28.94	28.97	28.87	28.89	28.99	28.99
28.61	28.64	28.56	28.64	28.74	28.74	28.62	28.64	28.82	28.84	28.66	28.62	28.64	28.67	28.71	28.69	28.62	28.65	28.71	28.62	28.61
28.55	28.61	28.47	28.50	28.45	28.50	28.56	28.43	28.54	28.54	28.53	28.49	28.53	28.47	28.45	28.52	28.49	28.54	28.45	28.51	28.44
28.25	28.17	28.25	28.19	28.18	28.15	28.22	28.17	28.23	28.30	28.27	28.26	28.22	28.22	28.31	28.24	28.20	28.14	28.20	28.31	28.22
28.10	28.06	28.06	28.05	28.05	27.99	28.05	28.01	28.11	27.97	27.97	28.05	28.15	27.98	28.07	28.00	27.99	27.91	28.08	28.04	28.08
27.78	27.83	27.74	27.74	27.78	27.84	27.85	27.88	27.74	27.75	27.89	27.75	27.79	27.75	27.73	27.67	27.81	27.75	27.85	27.66	27.81
27.48	27.53	27.53	27.56	27.50	27.48	27.60	27.57	27.53	27.48	27.53	27.55	27.55	27.65	27.53	27.50	27.61	27.58	27.62	27.51	27.50
27.36	27.36	27.34	27.42	27.34	27.28	27.36	27.34	27.47	27.35	27.37	27.41	27.41	27.31	27.31	27.36	27.39	27.35	27.28	27.39	27.48
27.14	27.13	27.22	27.16	27.13	27.24	27.08	27.10	27.12	27.17	27.23	27.12	27.14	27.14	27.08	27.14	27.13	27.15	27.06	27.12	27.14
26.49	26.87	26.87	26.83	26.95	26.81	26.85	26.87	26.87	26.88	26.96	26.91	26.79	26.90	26.82	27.03	26.90	26.85	26.87	26.88	26.87

FIGURE 25

The Range Image for a Crater at 30 m

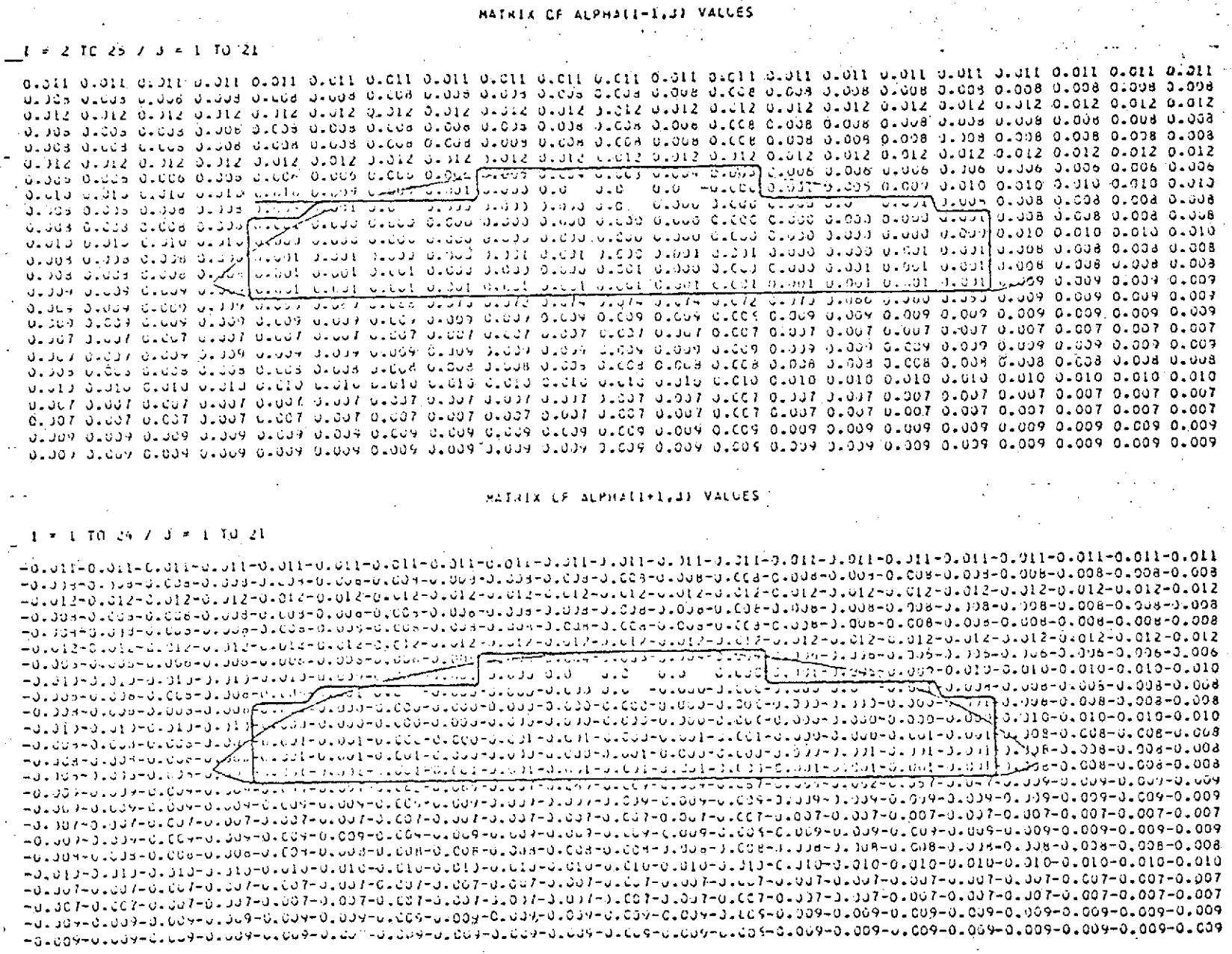

FIGURE 26

Two of the α Matrices for a Crater at 30 m

MATRIX OF ALPHA[I,J-1] VALUES

I = 1 TO 25 / J = 2 TO 21

MATRIX OF ALPHA[I,J+1] VALUES

I = 1 TO 25 / J = 1 TO 20

FIGURE 27

Two of the α Matrices for a Crater at 30 m

FOUR DIRECTIONAL RATIO EDGE DETECTION SCHEME, WITH N=2

1.00	1.00	1.00	1.00	1.00	1.00	1.00	1.00	1.00	1.00	1.00	1.00	1.01	1.00	1.00	1.00	1.00	1.01
1.00	0.99	1.00	1.00	1.00	1.00	1.00	1.00	1.00	0.99	1.01	0.99	1.00	1.00	1.00	1.00	1.00	1.00
1.00	1.00	1.00	1.01	1.00	1.00	1.00	1.00	1.00	1.01	1.00	1.00	1.01	1.00	1.00	1.00	1.01	0.99
1.00	1.00	1.00	1.00	1.00	1.00	1.01	1.00	1.00	1.00	1.01	1.01	1.00	1.00	1.00	1.00	1.00	1.00
1.00	1.00	1.00	0.99	1.00	1.00	1.00	0.99	1.00	1.00	0.99	1.00	1.00	0.99	1.00	0.99	1.00	1.00
1.00	1.00	1.00	1.00	1.00	1.00	1.00	1.00	1.00	1.01	1.00	1.01	1.00	1.00	1.00	1.01	1.00	1.00
1.00	1.00	1.00	0.99	1.01	1.00	1.00	1.01	1.00	1.00	1.00	1.01	1.00	1.00	1.00	1.00	0.99	1.00
1.00	1.00	0.99	1.01	1.00	0.99	1.01	1.00	1.00	1.00	1.01	1.00	1.00	1.00	1.01	1.01	1.00	1.00
1.00	1.00	1.00	1.01	0.99	1.00	1.00	1.00	1.00	1.00	1.00	1.00	1.00	1.00	1.00	1.01	1.00	1.00
1.00	1.00	1.00	1.00	1.00	1.00	1.00	1.00	1.01	1.00	1.00	1.00	1.01	1.00	1.00	1.00	1.00	1.00
1.00	1.00	1.01	1.01	1.01	1.00	1.00	1.00	1.00	1.00	1.01	0.99	1.00	1.00	1.00	0.99	1.01	1.00
1.00	1.00	1.01	0.99	1.00	1.00	1.00	1.00	1.00	1.00	1.00	1.00	1.00	1.00	1.00	0.99	1.01	1.00
1.00	1.00	1.01	0.99	1.00	1.00	1.01	1.00	1.00	1.00	1.00	1.00	1.00	1.00	1.00	0.99	1.01	1.00
1.00	1.00	1.02	0.98	0.98	0.98	0.97	0.97	0.98	0.97	0.97	0.97	0.97	0.97	0.98	1.02	1.01	1.00
1.00	1.00	1.00	1.01	1.01	1.01	1.01	1.01	1.01	1.01	1.01	1.01	1.01	1.01	1.02	1.00	1.01	1.00
1.00	1.00	1.00	1.00	1.00	1.01	1.00	1.00	1.01	1.00	1.00	1.00	1.00	1.00	1.01	1.00	1.00	1.01
1.00	1.00	1.00	1.00	1.00	0.99	1.00	1.00	1.00	1.00	1.00	1.00	1.00	1.00	1.00	0.99	1.00	1.00
1.01	1.00	1.00	1.00	1.00	1.00	1.00	1.00	1.00	1.00	1.00	1.00	1.00	1.00	1.00	1.01	1.00	1.00
1.00	1.00	1.00	1.00	1.00	1.00	1.00	0.99	1.00	1.00	1.00	0.99	1.00	1.00	1.00	1.01	0.99	1.00
1.00	1.00	1.00	1.00	1.00	1.00	0.99	1.01	1.00	1.00	1.00	1.00	1.00	1.00	1.01	1.00	1.00	0.99
1.00	1.00	1.00	1.00	1.01	1.00	1.00	1.00	1.00	1.00	1.00	1.00	0.99	1.00	1.00	1.00	1.00	1.00
1.00	1.00	1.00	1.00	1.01	1.00	1.00	0.99	1.00	1.00	1.00	1.00	1.00	1.00	1.00	1.00	1.01	1.00
1.00	0.99	1.00	1.00	0.99	1.00	1.00	1.00	1.00	0.99	1.00	1.00	1.00	1.00	1.00	1.00	1.00	1.00

NORMALIZED LAPLACIAN EDGE DETECTION SCHEME

0.00	-0.00	0.00	0.00	0.00	0.00	0.00	0.00	-0.00	0.00	0.00	-0.00	0.00	-0.00	0.00	0.00	0.00	0.00
-0.00	-0.00	-0.00	0.00	-0.00	-0.00	-0.00	-0.00	0.00	-0.00	0.00	-0.00	0.00	-0.00	0.00	-0.00	-0.00	-0.00
0.00	0.00	-0.00	0.00	0.00	0.00	-0.00	0.00	-0.00	0.00	-0.00	-0.00	0.00	0.00	-0.00	0.00	0.00	-0.00
0.00	-0.00	0.00	-0.00	-0.00	0.00	0.00	-0.00	0.00	-0.00	0.00	-0.00	-0.00	-0.00	-0.00	0.00	-0.00	0.00
0.00	-0.00	-0.00	-0.00	-0.00	0.00	0.00	-0.00	-0.00	-0.00	-0.00	-0.00	-0.00	-0.00	0.00	-0.00	-0.00	0.00
0.00	0.00	0.00	0.00	-0.00	0.00	0.00	0.00	0.00	0.00	0.00	0.00	0.00	0.00	-0.00	0.00	0.00	0.00
0.00	-0.00	0.00	-0.00	0.00	0.00	-0.00	-0.00	0.00	-0.00	-0.00	0.00	-0.00	0.00	-0.00	-0.00	0.00	-0.00
0.00	0.00	-0.00	0.00	0.00	-0.00	0.00	0.00	-0.00	-0.00	0.00	-0.00	0.00	-0.00	0.00	0.00	-0.00	0.00
-0.00	-0.00	0.00	0.00	-0.00	0.00	0.00	-0.00	0.00	0.00	-0.00	-0.00	0.00	-0.00	-0.00	0.00	-0.00	0.00
0.00	-0.00	0.00	0.00	-0.00	0.00	-0.00	-0.00	0.00	0.00	-0.00	-0.00	0.00	-0.00	-0.00	0.00	-0.00	0.00
-0.00	-0.00	0.01	-0.00	-0.00	0.00	0.00	-0.00	-0.00	-0.00	0.01	-0.00	-0.00	-0.00	-0.00	-0.00	0.01	-0.00
0.00	0.00	0.00	-0.00	-0.00	-0.00	-0.00	-0.00	0.00	-0.00	-0.00	0.00	-0.00	0.00	0.00	-0.00	0.00	-0.00
-0.00	0.00	0.00	-0.00	-0.00	-0.00	0.00	-0.00	-0.00	0.00	0.00	-0.00	0.00	-0.00	-0.00	0.01	-0.00	0.00
0.00	0.00	0.01	-0.00	-0.00	0.00	-0.00	-0.00	-0.00	-0.00	-0.00	-0.00	-0.00	-0.00	-0.00	0.00	0.00	-0.00
0.00	-0.00	0.00	0.01	0.01	0.01	0.01	0.01	0.01	0.01	0.01	0.01	0.01	0.01	0.01	-0.00	0.00	-0.00
0.00	0.00	0.00	-0.00	-0.00	0.00	0.00	-0.00	0.00	0.00	0.00	0.00	0.00	-0.00	-0.00	0.00	0.00	0.00
-0.00	0.00	-0.00	0.00	-0.00	-0.00	0.00	0.00	-0.00	-0.00	-0.00	-0.00	0.00	0.00	-0.00	-0.00	-0.00	0.00
0.00	-0.00	0.00	0.00	0.00	0.00	0.00	0.00	-0.00	-0.00	0.00	0.00	0.00	-0.00	0.00	0.00	-0.00	-0.00
-0.00	-0.00	0.00	-0.00	0.00	-0.00	0.00	-0.00	0.00	0.00	0.00	-0.01	0.00	-0.00	-0.00	0.00	0.00	-0.00
-0.00	0.00	0.00	-0.00	-0.00	-0.00	-0.00	0.00	-0.00	0.00	0.00	0.00	0.00	0.00	0.00	-0.00	0.00	0.01
0.00	0.00	-0.00	0.00	0.00	0.00	0.00	0.00	0.00	-0.00	0.00	0.00	-0.00	0.00	-0.00	-0.00	0.00	0.00
-0.00	-0.00	-0.00	-0.00	0.00	-0.00	0.00	-0.00	0.00	-0.00	0.00	-0.00	0.00	0.00	0.00	-0.00	0.00	0.00
0.00	-0.00	-0.00	0.00	-0.01	0.00	0.00	0.00	-0.00	-0.00	0.00	-0.00	0.00	0.00	0.00	-0.00	0.00	0.00

FIGURE 28

The Edge Detection Matrices for a Crater at 30 m

EDGE ENHANCEMENT BASED ON FOUR DIRECTIONAL RATIO (N=2)

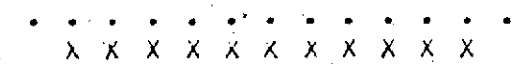

EDGE ENHANCEMENT BASED ON NORMALIZED HAMILTONIAN

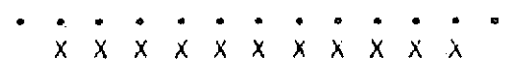

FIGURE 29

Outlines of the Crater at 30 m

SUMMARY AND CONCLUSIONS

The research detailed in this paper was directed toward the development of a practical obstacle detection system for the Mars Rover. A simple scheme was desired, which would operate on the raw data obtained from the laser rangefinder mounted on the Rover in order to enhance the outline of an obstacle in the vehicle's path. By this means the size and location of the obstacle can be determined, and this information used to make path selection decisions. Such a scheme was devised and simulated for a number of typical obstacles, and the results indicate that it has a high practical potential. Yet, as with any initial venture of this kind, as questions are answered even more questions are raised. Problems such as bottom edge detection and scanning scheme determination remain to be solved. Thus, this project should be seen as the first encouraging steps toward realization of the final operating system.

REFERENCES

1) "An Exploratory Investigation of a 1973 Mars Roving Vehicle Mission", [illegible], Jet Propulsion Laboratory, California Institute of Technology, Pasadena, California.

2) Pavarini, C. and Chrysler, J.H., "Terrain Modeling and Path Selection by an Autonomous Martian Exploratory Vehicle", R.P.I. Technical Report MP-14, NASA Grant 33-018-191, June 1970.

3) "Analysis and Design of a Capsule Landing System and Surface Vehicle Control System for Mars Exploration", R.P.I. 1973-74 Proposal, NASA Grant NGL 33-018-091.

4) Kirk, D.E. and Lim, L.Y., "A Dual-mode Routing Algorithm for an Autonomous Roving Vehicle", IEEE Transcript on Aerospace and Electronic Systems, Volume AES-6, No. 3, May 1970.

5) Shen, C.N. and Berger, P., "Stochastic Estimates of Gradient From Laser Measurements for an Autonomous Martian Roving Vehicle", Proceedings of the Third IFAC Symposium, The Hague/Delft, The Netherlands, June 1973.

6) Shen, C.N. and D'Angelo, K.R., "Parameter Estimation for Martian Terrain Modeling from Gradient Data", Seventh Hawaii International Conference on System Sciences, Honolulu, Hawaii, January, 1974.

7) Neuberger, A., "Characterization of Pictures by Essential Contours", M.S. Thesis, M.I.T., 1966.

8) Reed, M., Sanyal, P., and Shen, C.N., "A Practical Obstacle Detection System for the Mars Rover", Second Annual Milwaukee Symposium on Automatic Control, Milwaukee, Wisconsin, March 1974.